Volume 7 Number 1 Jan - Mar 2018

STUDENT JOURNAL OF PHYSICS

INTERNATIONAL EDITION

INDIAN ASSOCIATION OF PHYSICS TEACHERS

ISSN – 2319-3166

STUDENT JOURNAL OF PHYSICS

This is a quarterly journal published by Indian Association Of Physics Teachers. It publishes research articles contributed by Under Graduate and Post Graduate students of colleges, universities and similar teaching institutions, as principal authors.

Registered Office

Editor-in-Chief, SJP, Institute of Physics, Sainik School, Bhubaneswar, Odisha, India – 751005
(www.iopb.res.in/~sjp/)

STUDENT JOURNAL OF PHYSICS

Scope of the Journal

The journal is devoted to research carried out by students at undergraduate level. It provides a platform for the young students to explore their creativity, originality, and independence in terms of research articles which may be written in collaboration with senior scientist(s), but with a very significant contribution from the student. The articles will be judged for suitability of publication in the following two broad categories:

1. **Project based articles**
   These articles are based on research projects assigned and guided by senior scientist(s) and carried out predominantly or entirely by the student.
2. **Articles based on original ideas of student**
   These articles are originated by the student and developed by him/ her with possible help from senior advisor. Very often an undergraduate student producing original idea is unable to find a venue for its expression where it can get due attention. SJP, with its primary goal of encouraging original research at the undergraduate level provides a platform for bringing out such research works.
   It is an online journal with no cost to the author.

Since SJP is concerned with undergraduate physics education, it will occasionally also publish articles on science education written by senior physicists.

Information for Authors

- Check the accuracy of your references.
- Include the complete source information for any references cited in the abstract. (Do not cite reference numbers in the abstract.)
- Number references in text consecutively, starting with [1].

- Language: Papers should have a clear presentation written in good English. Use a spell checker.

Submission

1. Use the link "Submit" of Website to submit all files (manuscript and figures) together in the submission (either as a single .tar file or as multiple files)
2. Choose one of the Editors in the link "Submit" of Website as communicating editor while submitting your manuscript.

Preparation for Submission

Use the template available at "Submit" section of Website for preparation of the manuscript.

Re-Submission

- For re-submission, please respond to the major points of the criticism raised by the referees.
- If your paper is accepted, please check the proofs carefully.

Scope

- SJP covers all areas of applied, fundamental, and interdisciplinary physics research.

STUDENT JOURNAL OF PHYSICS

Networks of topological string defects with different Non-Abelian fundamental groups

Ramyak Bilas[1] *

[1]3rd year BS-MS, Indian Institute of Science Education and Research, Kolkata, Mohanpur, Nadia, WB, India, 741246

Abstract. Topological string defects corresponding to a non-Abelian fundamental group have interesting property of entanglement thus giving rise to the possibility of network formations. We consider some conventional as well as some hypothetical non-Abelian fundamental groups and investigate possibility of different types of networks in each case. The network structures we discuss are one of these three : Hexagonal, Cubic and Diamond lattice.

Keywords: Topological defects, Mean-Abelian fundamental group, String crossing, Biaxial nematics.

1. INTRODUCTION

An ordered media is characterised by an order parameter associated at each point of the system. The collection of all possible values of order parameters gives us an order parameter space. It can be argued on the grounds of topology that certain arrangements of the order parameter produce singularities that cannot be removed by local deformations. Such defects that arise entirely due to topology are called topological defects. These are then categorised into monopole defects, string defects ,etc. Here our primary interest lies in string defects. As we shall see, in certain cases of media(non-Abelian) line defects get entangled i.e. when we cross one string defect around other there remains behind a link joining the two defects at the crossing points. If the topology of the order parameter space (specifically, the structure of its fundamental group) allows it, we can have three or more links at a given point on a string defect giving rise to the possibility of network structures. Almost all the cases that we shall consider here have symmetry groups that have not been observed apart from the case of biaxial nematics (D_2 point group symmetry). Biaxial nematic ordering is expected to arise in certain liquid crystal systems, though it has never been observed as a thermotropic liquid crystal phase. For most of the discussion here, we have followed ref. [1]

** rb16ms027@iiserkol.ac.in

2. CLASSIFYING STRING DEFECTS

2.1 *ORDER PARAMETER SPACE AS COSET SPACE*

Every ordered media has associated with it a function that assigns with each point of space a specific value of an order parameter. Additionally all such order parameter values have associated with them 'a group of transformation G, such that if f_1 and f_2 are any two possible values of the order parameter then there exist a group element g such that $f_2 = gf_1$.' Fixing f, if we define H to be the set of all g such that $gf = f$, then H forms a subgroup of G called as the isotropy group of f. It can be shown that there is an one-one correspondence between elements of order parameter space and elements of coset space G/H giving us a powerful description of the order parameter space.

2.2 *FUNDAMENTAL GROUP*

If we consider loops in physical space then we get corresponding loops in the order parameter space R. If we have a single special value of the order parameter (say x) fixed in those loops then we get based loops. Homotopy classes of such based loops form a group structure. (For this to hold the order parameter space must be path connected.) This is called as the fundamental group of R, or the first order homotopy group $\pi_1(R, x)$.

2.3 *CONJUGACY CLASSES*

The elements of $\pi_1(R, x)$ each depicts a kind of line defect. These essentially should not be able to convert to one another by continuous transformation. But as we have imposed the condition that one point x to be fixed to impose a group structure, we have not exhausted all possibilities of conversion by smooth deformations. The construct of having a fixed point in the loop is artificial and there should indeed be no restriction on such loops apart from the fact that the loops in physical space must surround the defects. For this we invoke a result that links the point based homotopy classes to the 'free homotopy classes'. A loop f at x is freely homotopic to a loop g at y if there is a path isomorphism c taking homotopy class $[f]$ of $\pi_1(R, x)$ into the homotopy class $[g]$ of $\pi_1(R, y)$.' This actually rearranges elements of $\pi_1(R)$ and the sets within which there is shuffling are the conjugacy classes. Thus elements of same conjugacy class can be converted to one another by taking them around another defect, while elements belonging to different conjugacy classes can never be converted to each other by smooth deformations and hence are genuinely topologically distinct defects. Thus a given conjugacy class of the fundamental group describes the set of all the inter-convertible string defects.

2.4 *FUNDAMENTAL THEOREM ON FIRST HOMOTOPY GROUP OF COSET SPACE*

In general, it is very difficult to directly compute $\pi_1(R)$. But a very important result lets us calculate it with much more ease:'If G is a connected and simply connected group, H is any subgroup of

G and H_0 is the set of points in H that are connected to the identity by continuous paths lying in H, then H/H_0 is isomorphic to the fundamental group $\pi_1(G/H)$ i.e. $\pi_1(G/H) \sim H/H_0$.' Thus calculating the fundamental group reduces to calculation of H/H_0.

3. EXAMPLES OF STANDARD AND HYPOTHETICAL FUNDAMENTAL GROUPS

3.1 *ORDINARY SPIN*

This order parameter space consisting of 3 dimensional unit vectors is found in variety of systems with the most widely known being the magnetisation of a ferromagnetic material. Here the group G can be taken to be $SO(3)$. H then is simply $SO(2)$. Thus we have $R = G/H$. But $SO(3)$ is not simply connected debarring us from use of the fundamental theorem. If we take $SU(2)$ then we have $R = SU(2)/U(1)$ where $U(1)$ is the lift of $SO(2)$ in $SU(2)$.But we have $U(1)$ which is connected to identity. Thus, $\pi_1(SU(2)/U(1)) = 0$. Thus there are no topological line defects in such a medium.

3.2 *NEMATIC LIQUID CRYSTALS*

In nematic liquid crystals G can be taken to be $SO(3)$ while H would then be D_∞ as their symmetry group is same as that of cylinder. If D'_∞ is the lift of D_∞ in $SU(2)$, it turns out that D'_∞ has two connected components. So, $\pi_1(SU(2)/D'_\infty) = Z_2$. Thus we have a non trivial defect and the fundamental group of the order parameter space is Abelian.

3.3 *BIAXIAL CRYSTALS*

These have a symmetry of rectangular box with point group D_2. Thus order parameter space $R = SO(3)/D_2$. The lift of D_2 in $SU(2)$ is isomorphic to quaternion group, $Q = \{\pm 1, \pm i\sigma_x, \pm i\sigma_y, \pm i\sigma_z\}$, where $\sigma'_i s$ are Pauli matrices. If the group H is discrete then $H/H_0 = H$. Thus we have $\pi_1(SU(2)/Q) = Q$. As Q is non-Abelian, biaxial nematics are thus non-Abelian. These split into five conjugacy classes: $\{1\}, \{-1\}, \{\pm i\sigma_x\}, \{\pm i\sigma_y\}, \{\pm i\sigma_z\}$.

Following two examples of fundamental group have been discussed in ref.[2].

3.4 *TRIANGULAR SYMMETRY*

If the order parameter has a D_3 symmetry group, the order parameter space would then be $R = SO(3)/D_3$. The lift of D_3 in $SU(2)$ is given by $D'_3 = \{\pm 1, \pm\omega, \pm\omega^2, \pm j, \pm j\omega, \pm j\omega^2\}$ where $j = -i\sigma_x$ and $\omega = -\frac{1}{2} - \frac{\sqrt{3}}{2}\sigma_z$. Just like above we conclude $\pi_1(SU(2)/D'_3) = D'_3$. This also turns out to be non-Abelian and has six conjugacy class: $\{1\}, \{-1\}, \{\omega, \omega^2\}, \{-\omega, -\omega^2\}, \{j, j\omega, j\omega^2\}, \{-j, -j\omega, -j\omega^2\}$. Thus we have five different kind of non-trivial defects that cannot inter-convert, see ref.[2] for details.

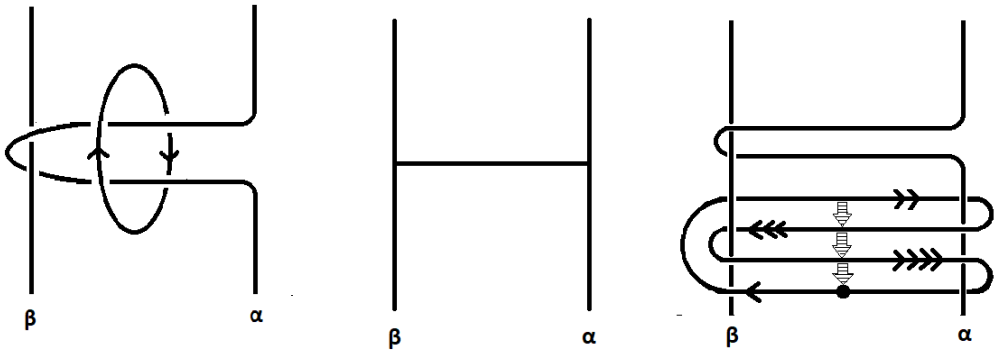

(a) (b) (c)

Figure 1.: Finding homotopy class of links formed by entangled strings

3.5 *OCTAHEDRAL SYMMETRY*

If order parameter has tetrahedral symmetry group, then $R = SO(3)/T$ where T is the chiral tetrahedral group. The lift of T in $SU(2)$ splits into seven conjugacy classes:$\{1\}, \{-1\}, \{\pm\alpha, \pm\beta, \pm\alpha\beta\}, \{\gamma, -\alpha\gamma, \beta\gamma, -\alpha\beta\gamma\}, \{-\gamma, \alpha\gamma, -\beta\gamma, \alpha\beta\gamma\}, \{\gamma^2, \alpha\gamma^2, -\beta\gamma^2, \alpha\beta\gamma^2\}, \{-\gamma^2, -\alpha\gamma^2, \beta\gamma^2, -\alpha\beta\gamma^2\}$, where $\alpha = \frac{1}{\sqrt{3}}\sigma_x + \frac{1}{\sqrt{6}}\sigma_y - \frac{1}{\sqrt{2}}\sigma_z$, $\beta = -\frac{1}{\sqrt{3}}\sigma_x - \frac{1}{\sqrt{6}}\sigma_y - \frac{1}{\sqrt{2}}\sigma_z$ and $\gamma = -\frac{1}{2} - \frac{\sqrt{3}}{2}\sigma_x$, see ref.[2] for details.

4. ENTANGLEMENT OF LINE DEFECTS

4.1 *NON-ABELIAN MEDIA AND ENTANGLEMENT*

Let us consider a simple exercise for two line defects that aren't exactly coplanar. If we try to cross one string defect α around the other defect β then we arrive at a configuration similar to figure 1(a). We can pinch the overlapping parts to get a construct like figure 1(b). It may so happen that this pinched defect may vanish then we simply recover our original configuration. But if it happens to be non-trivial then we are left with a link between the two line defects and arrive at the so called 'entanglement' of line defects.

To determine the homotopy class of the link consider a loop around it and deform it to arrive at a configuration similar to figure 1(c). We conclude that the class of the link is $\beta \circ \alpha \circ \beta^{-1} \circ \alpha^{-1}$. A similar exercise (in figure 2) suggests that the upper half of α changes to $\beta \circ \alpha\beta^{-1}$. The link is trivial if $\alpha \circ \beta = \beta \circ \alpha$ i.e. medium is Abelian. Thus we can only have non-trivial links in case of non-Abelian media. (When we say the medium is Abelian or non-Abelian, we mean that the fundamental group of the corresponding order parameter space is Abelian or non-abelain respectively.)

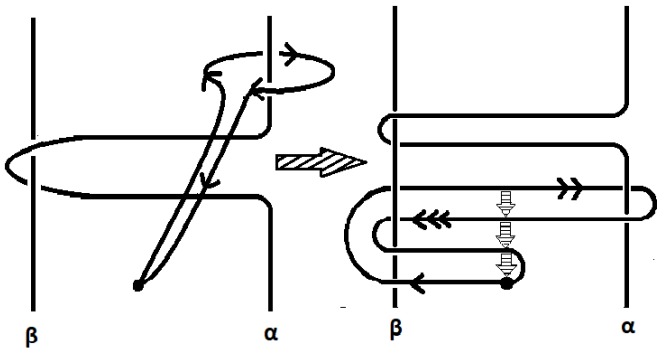

Figure 2.: Finding homotopy class of string after crossing the other string

4.2 *PROPERTY OF THE CLASS THE LINKS BELONG TO*

If σ is a link i.e. $\exists\ \alpha$ and β such that $\alpha \circ \beta \circ \alpha^{-1} \circ \beta^{-1} = \sigma$, then all the elements of the conjugacy class that σ belongs to are valid links too .To frame the claim mathematically: If $\sigma' \in A$ where A is the conjugacy class of σ, then $\exists\ \alpha'$ and β' such that $\alpha' \circ \beta' \circ \alpha'^{-1} \circ \beta' - 1 = \sigma'$.

The above statement is true because: $\gamma \circ \{\alpha \circ \beta \circ \alpha^{-1} \circ \beta^{-}1\} \circ \gamma^{-1} = \{\gamma \circ \alpha \circ \gamma^{-1}\} \circ \{\gamma \circ \beta \circ \gamma^{-1}\} \circ \{\gamma \circ \alpha^{-1} \circ \gamma^{-1}\} \circ \{\gamma \circ \beta^{-1} \circ \gamma^{-1}\} = \alpha' \circ \beta' \circ \alpha'^{-1} \circ \beta'^{-1}$

Another important observation about the conjugacy classes that such links may belong to is the fact that the conjugacy class must contain inverses of all of its elements i.e. if $\alpha \in A \implies \alpha^{-1} \in A$ where A is the conjugacy class. This is an observation without proof. This seems to be a necessary condition but not a sufficient one for a conjugacy class to produce links.

5. LINKS POSSIBLE IN VARIOUS NON-ABELIAN MEDIA

If we have a non-Abelian media then we are guaranteed to get atleast one conjugacy class of links (simply because if no such link exist then it means that the group is Abelian). Thus even in case of the most trivial non-Abelian media we are guaranteed to get links connecting various line defects. The following text describes the kind of links as well as when they form in the specific non-Abelian media. We shall use $\longrightarrow$ to mean first string crosses the other.

5.1 *Biaxial Nematic Liquid Crystal*

From multiplication table of the quaternion group, $\beta \circ \alpha \circ \beta^{-1} \circ \alpha^{-1}$ can only be either 1 or -1. The non-trivial -1 link forms when $\pm\sigma_i \longrightarrow \pm\sigma_j$ such that $i \neq j$ and the α (i.e. the one that crosses) changes sign. Thus we have only one kind of link in biaxial nematic.

5.2 *Triangular Symmetry*

Here we have a bit more diversity then previous case as links can be trivial or ω or ω^2. We have ω link if $\pm\omega \longrightarrow \{j, j\omega, j\omega^2\}, \{-j, -j\omega, -j\omega^2\}$; $\{j, j\omega, j\omega^2\}, \{-j, -j\omega, -j\omega^2\} \longrightarrow \pm\omega^2$; $\pm j \longrightarrow \pm j\omega$; $\pm j\omega \longrightarrow \pm j\omega^2$ or $\pm j\omega^2 \longrightarrow \pm j$. To get a ω^2 link we can cross the following: $\pm\omega^2 \longrightarrow \{j, j\omega, j\omega^2\}, \{-j, -j\omega, -j\omega^2\}$; $\{j, j\omega, j\omega^2\}, \{-j, -j\omega, -j\omega^2\} \longrightarrow \pm\omega$; $\pm j \longrightarrow \pm j\omega^2$; $\pm j\omega^2 \longrightarrow \pm j\omega$ or $\pm j\omega \longrightarrow \pm j$. The upper half of the crossing link can be computed by calculating $\beta\alpha\beta^{-1}$.

5.3 *Octahedral Symmetry*

This fundamental group has got a very complicated crossing and varied classes of links. The links can belong to either $\{-1\}$ or $\{\pm\alpha, \pm\beta, \pm\alpha\beta\}$. The α and β in this case is very complicated. We can have -1 only when $\{\pm\alpha, \pm\beta, \pm\alpha\beta\}$ crosses members of itself in certain cases. The other links form when other conjugacy classes cross among each other where in some cases we get trivial links. This increases our pool of distinct classes of links to seven. As we shall see it provides a good set to form $3-$dimensional lattice of networks.

6. NETWORKS POSSIBLE IN VARIOUS MEDIA

The previous section gives us a possibility of forming networks of defects. This section gives a detailed understanding of the types as well as the expected stability of different structures.

6.1 *STITCHING PATTERN*

The way in which we 'stitch' the defects affects the overall stability of the network that we construct. By 'stitching' we mean the manner and order in which the links are formed and stacked. The way we do it is analogous to how we weaves a piece of cloth and the whole arrangement of thread holds its shape and not separate into a mass of independent threads. As we shall see the networks that we construct 'remembers the way it was stitched and thus maintains its overall structure and this stability is topological i.e. it's stability does not depend on the energetics rather is intrinsic to the medium itself. So it is important to define a proper way of stitching that if constructed for threads would maintain the structure.

6.2 *NON-CROSSING OF LINKS*

The links are formed when one string crosses the other. Thus links are independent entity. When stacked upon each other we get numerous links at a particular node. It is important to note that the links should be such that they can't bypass each other and always maintain the order in which they we stitched. In most cases the above statement is true. But there exist cases where the above

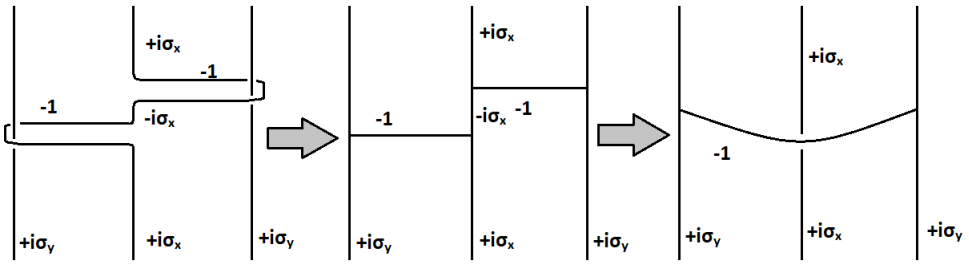

Figure 3.: Possible untangling of links

statement is false. So while looking at networks of defects it is important that links don't bypass each other so that it maintains the structure the way these were put together.

6.3 *POSSIBLE LATTICE OF DEFECTS*

Keeping in mind the above points and the fact that we should avoid stacking up same classes of defects consecutively we can have the following basic lattices.

6.3.1 *HEXAGONAL LATTICE*

Let us consider the simplest of all the non-Abelian fundamental group, biaxial nematic. As we have only one class of link i.e $\{-1\}$ possible so it rules out the possibility of more than one branch at a particular node made by a single string.

As shown in figure 3, there is a possibility of the links separating out if we have two branch originating from the same string at a node. So it is wise to opt for a safe one branch network. If 'tension' remains constant then the most stable network is that of a 2-D hexagonal lattice.

It is important to note the stitching pattern as this is an important factor in deciding stability of the network. The scheme is shown in figure 4.

In figure 4, each branch from a string is sandwiched between two branch of the adjacent string . So, if we try to separate out a link by joining two -1 links as done previously we shall end up with a point where we have two distinct class of defects in point based homotopy group joining which contradicts the very meaning of being distinct class in a point based homotopy group. As we can see in figure 5, we have a continuity problem for the string that changes from $-i\sigma_x$ to $+i\sigma_x$.

As shown in figure 4, the consecutive string defects belong to different conjugacy classes. In fact our only requirement in this case is to have no two adjacent string defects belonging to same conjugacy class and the choice can be completely random which still remains topologically stable. Thus we can have infinite such arrangements.

We can rearrange the stitching in figure 4 to get a 2-D square lattice as in figure 6.

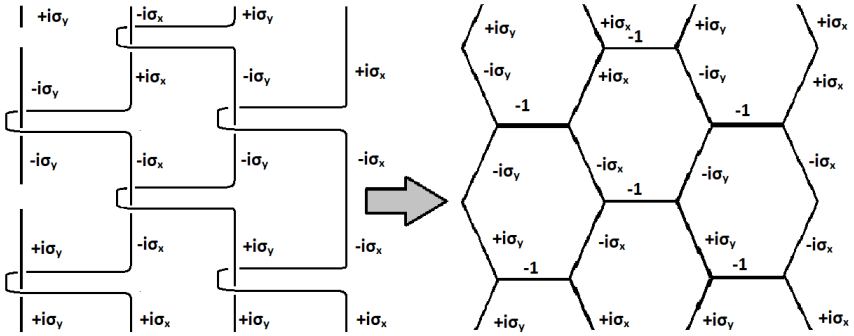

Figure 4.: Stitching pattern for 2-D hexagonal lattice

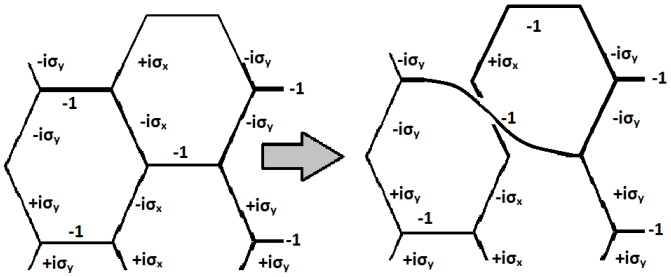

Figure 5.: Infeasibility of untangling the links

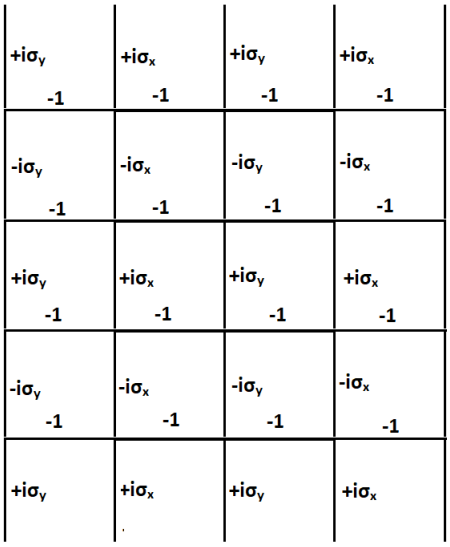

Figure 6.: 2-D square lattice with biaxial nematic

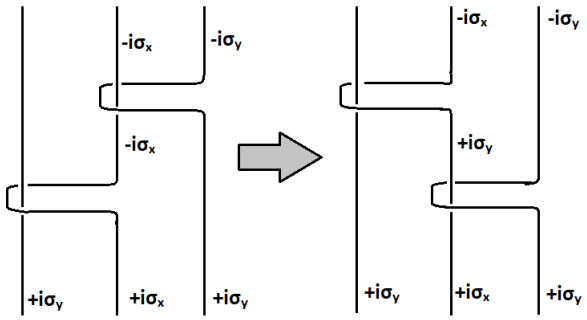

Figure 7.: Sliding of links

As the stitching which forms the cubic lattice is topologically stable so is the lattice formed by sliding links.

However links here can cross each other as in figure 7. Thus we have some kind of mobility in the stitching we did for biaxial nematic.

This can be overcome and a perfectly non-mobile topologically stable stitching can be obtained if we use fundamental group of triangular or octahedral symmetry.(Refer figure 8)

Here in figure 8 the string 1 shows a periodic change from j to $j\omega$ to $j\omega^2$ while string 2 alternates between ω and ω^2. As can be verified, it overcomes the previous problems of link mobility.

The hexagonal crossing can have a variants too.

In pattern 1 (refer figure 9), we have a general way of building hexagonal lattice. We trace a line in the hexagonal lattice such that if we add up the angle we turn its absolute value should not exceed 180^0. This allows us to stack up the same pattern on top of one another. Pattern 2 uses the same principle while making use of the 180^0 change in direction of defects. In pattern 3 we have the angle of turns add up to be greater than 180^0 so that the next defect covers more space and thus we have a family of defects of increasing width. As can be noted one string must cross itself for it to form the lattice but one class commutes with itself so that we have no links along their contact barring the formation of complete lattice.

6.3.2 *CUBIC LATTICE*

We directly make use of the largest non-Abelian fundamental group at our disposal to show the feasibility of cubic lattice. Our requirement for stability of the structure is that neither stitching should not crumble upon itself nor should the links be mobile as noted earlier. Avoiding those two points ensures topological stability.

In case of tetrahedral symmetry, we have two different two different conjugacy class of links as well as seven different classes of them. For the sake of simplicity, we shall make use of only one conjugacy class i.e. $\{\pm\alpha, \pm\beta, \pm\alpha\beta\}$. Thus we have more freedom of stacking up links. We shall

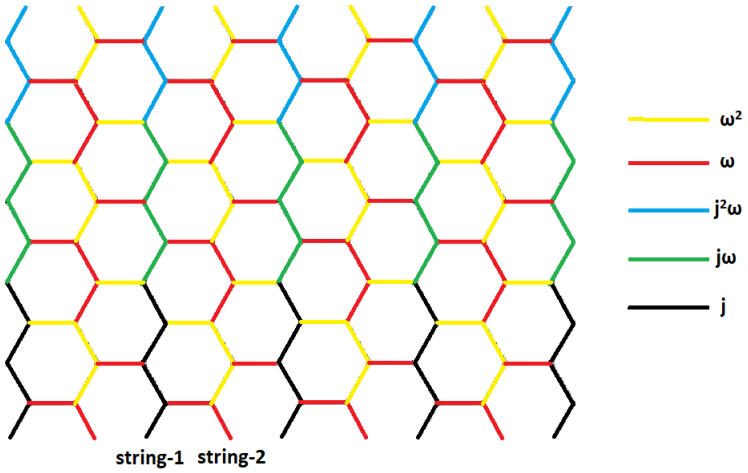

Figure 8.: 2-D hexagonal lattice formed with fundamental group of triangular symmetry

adopt a similar stitching as in hexagonal lattice(refer figure 10).

Figure 11 shows two layers of such a structure. These two layers sandwich each other and form the whole of the cubic lattice as shown in Figure 14. Each node has different links. As can be verified the links can neither be untangled nor crossed across each other. So it's a topologically stable structure. We can choose elements of other conjugacy classes too to get a similar structure.

6.3.3 *DIAMOND LATTICE*

The stitching used in forming cubic lattice can be easily changed to a diamond lattice (refer figure 13). The model shown in figure 13 is made using wires and colour coded using tapes to identify various classes of string defects. This is similar with what we did with 2-D hexagonal to square lattice.

6.4 *POSSIBILITY OF OTHER NETWORKS*

We have only explored the lattices which would have a constant tension throughout. But the number of lattice possible is theoretically infinite, depending on differences in tensions of different strings. But the fact that we have to trace out lines apart from the links to completely make that structure should be kept in mind. Apart from standard lattice we can do a bit more with the fundamental group of the tetrahedral symmetry. If we choose our strings to be γ and $\alpha\beta\gamma^2$ then we can build bilayers using the stitching as used in cubic lattice because these change into $-\alpha\beta\gamma$ and $\alpha\gamma^2$ respectively (refer figure 14). Then we can stitch in an inverted way below also to get a topologically stable structure. We can take various other elements to get the required result as in other cases.

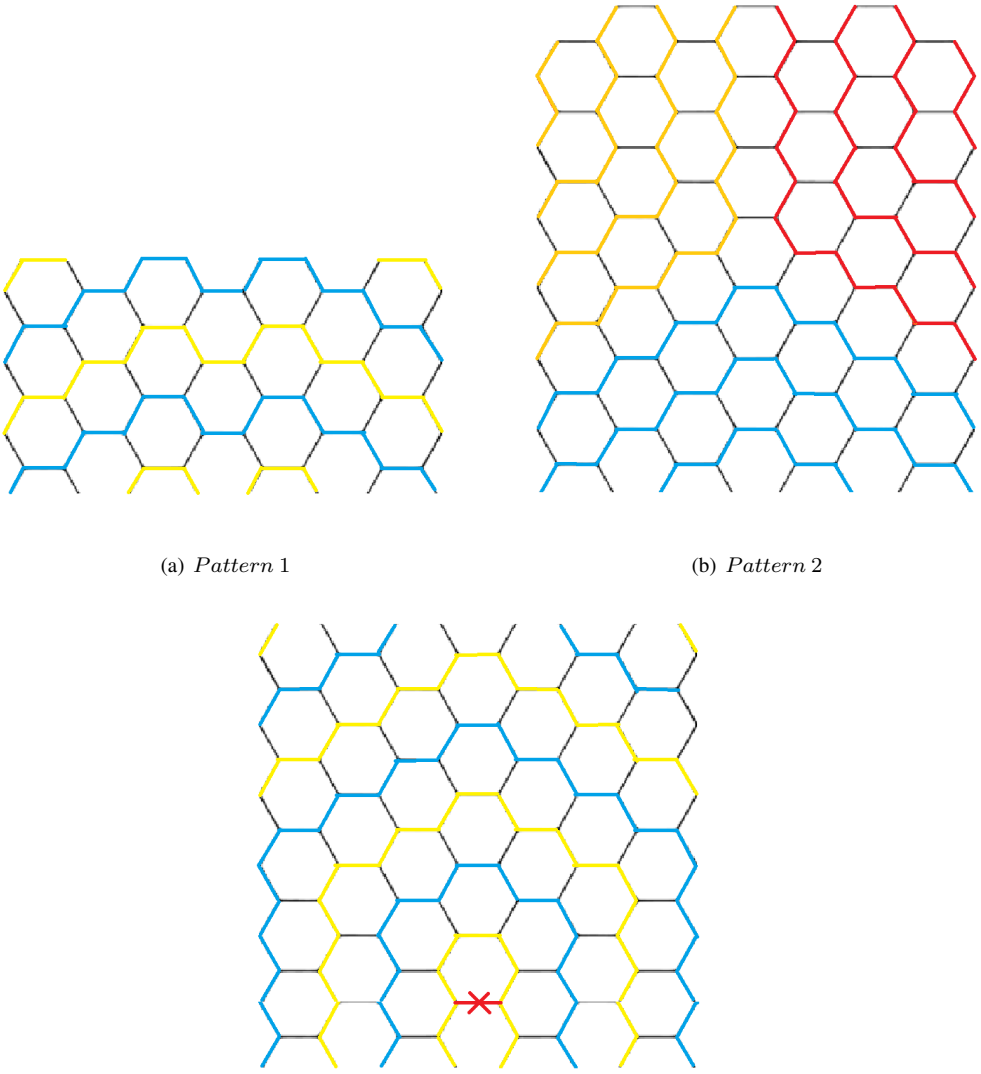

(a) *Pattern* 1

(b) *Pattern* 2

(c) *Pattern* 3

Figure 9.: Variants of 2-D hexagonal lattice

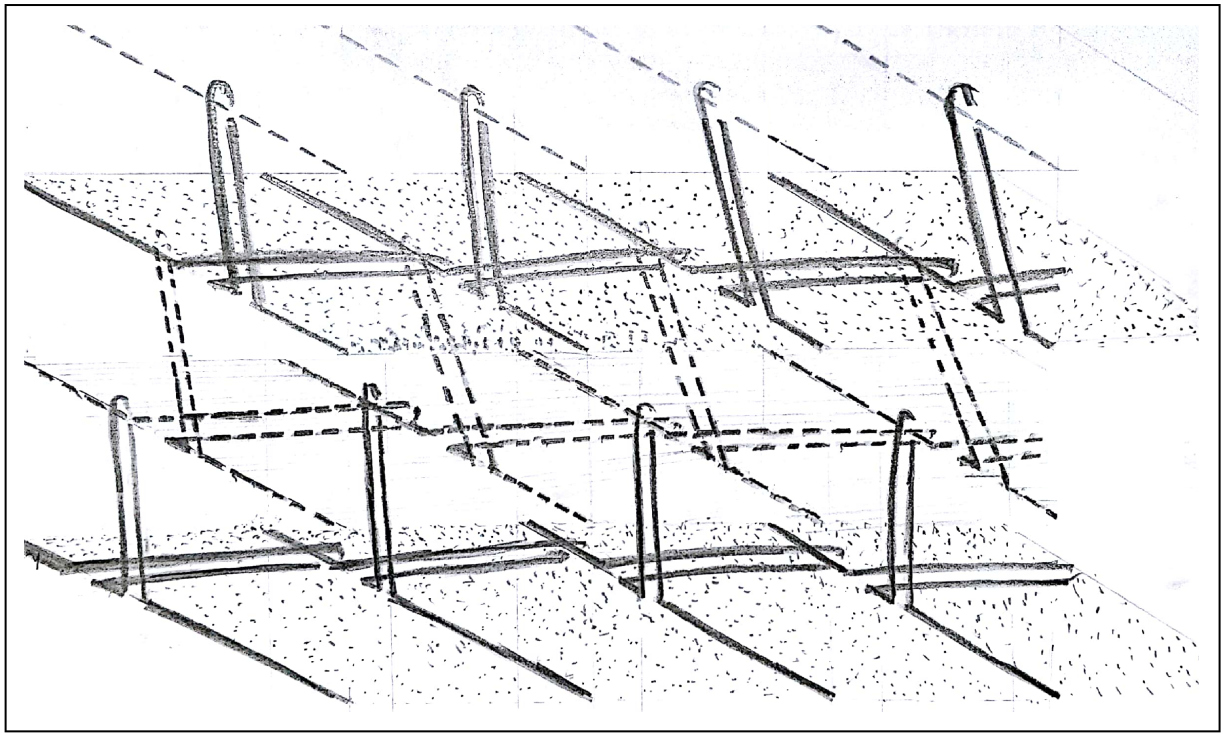

Figure 10.: Stitching patten for cubic lattice

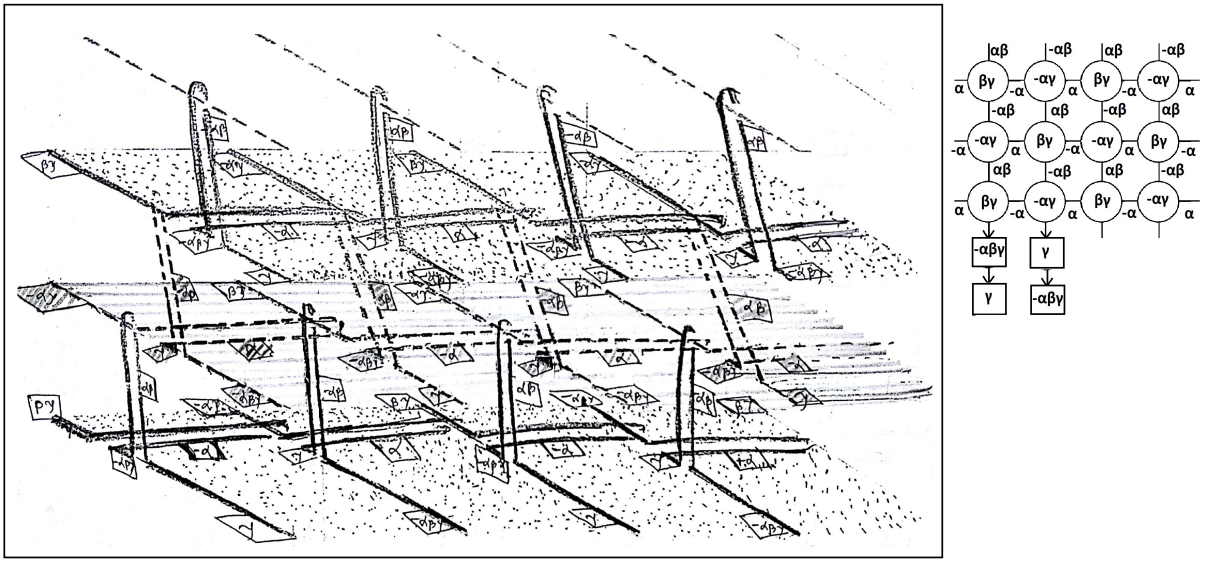

(a) *Layer* 1

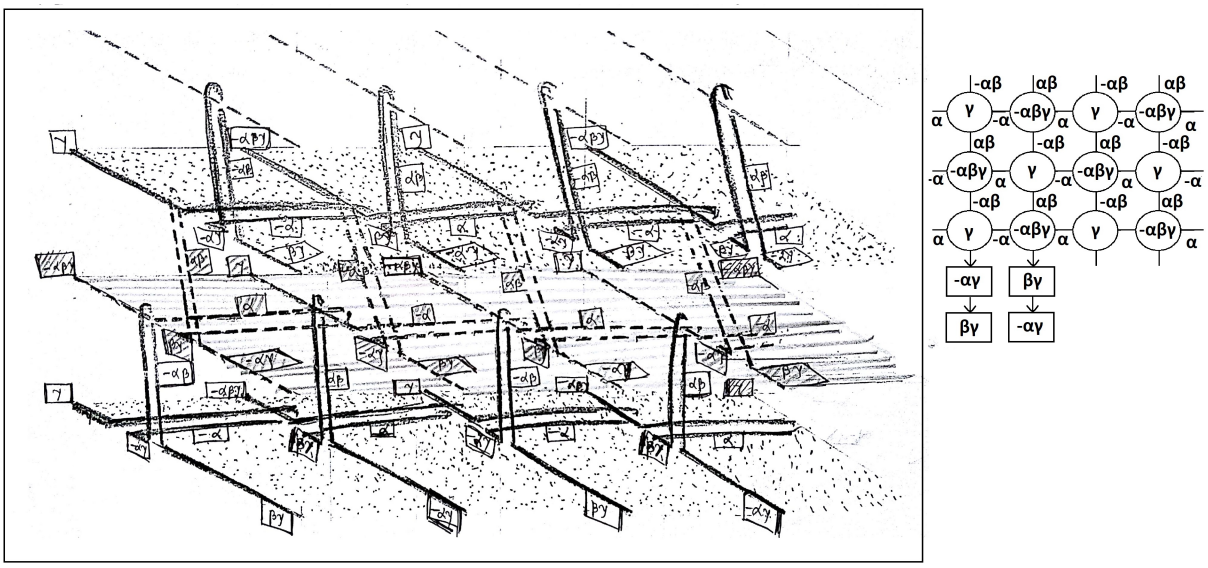

(b) *Layer* 2

Figure 11.: Layers of a cubic lattice

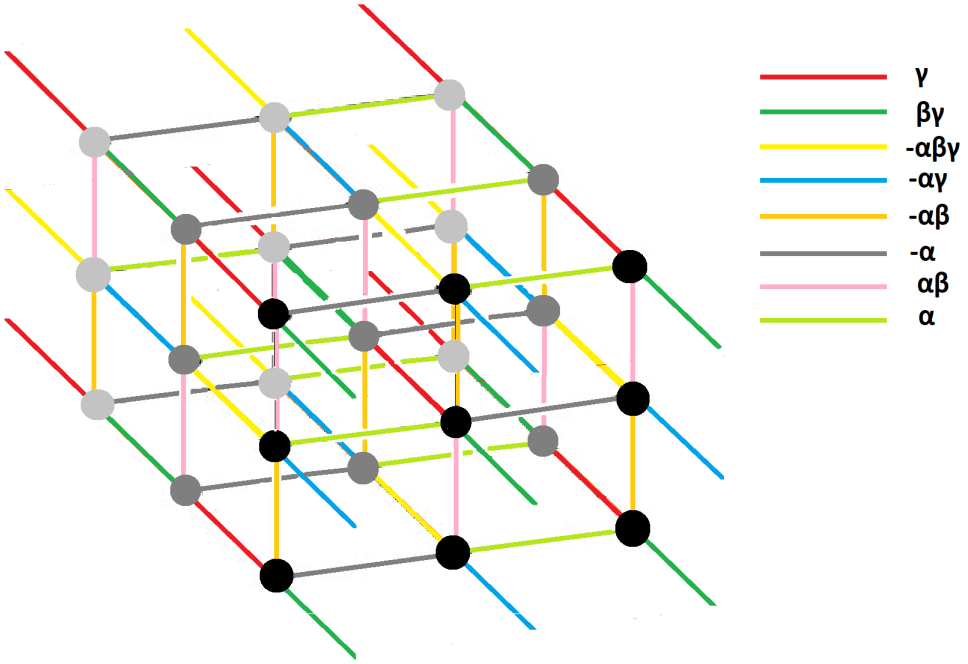

Figure 12.: Layers of a cubic lattice

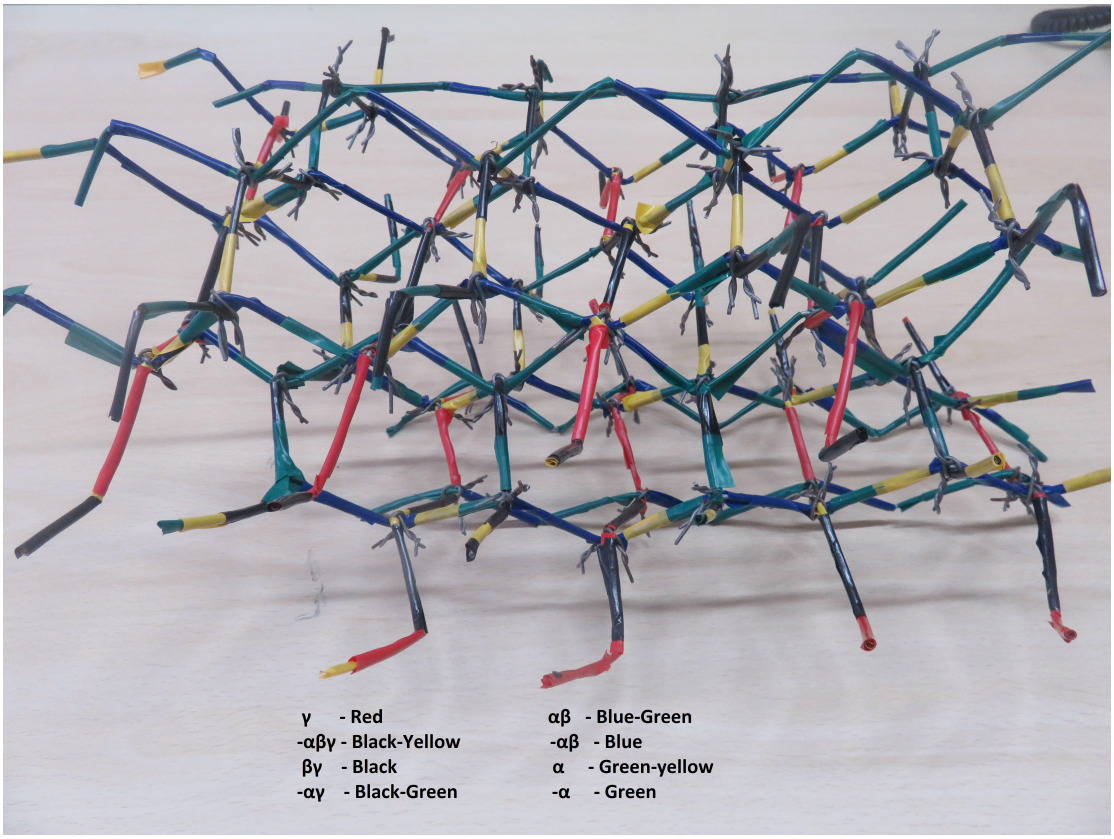

Figure 13.: Diamond lattice

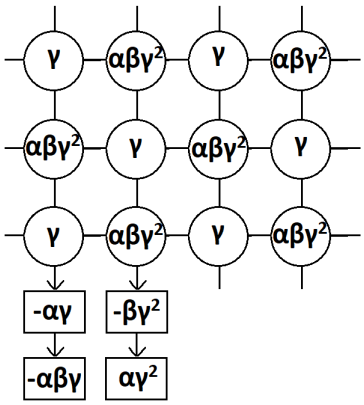

Figure 14.: Block diagram for bilayer

If we have fundamental groups of higher order symmetry then we can build more complicated nodes. Here in the example we used for cubic and diamond lattice have only two layers that repeat and each layer has only two different kinds of sting. We can in fact use more number of strings of different classes and in turn get periodicity of varying order.

7. CONCLUSION

To conclude, we have demonstrated topological stability of network structures formed from string defects in an non-Abelian medium. The diversity of classes in the fundamental group largely affects the variety of networks possible. As has been noted above, ensuring the stability of the stitching pattern used to construct a network ensures the network's stability. An ordered media such as liquid crystal or ferromagnetic materials are largely affected by the presence or absence of defects in them. In case of biaxial nematic liquid crystals or other symmetry groups (if discovered) could allow for more control over the distribution of defects by formation of networks of them affecting the material properties. Thus in those cases such networks might play an crucial role in material science.

ACKNOWLEDGEMENT

I am very grateful to Prof. Ajit M. Srivastava for suggesting this project to me and for guiding me throughout. I am grateful to Institute of Physics, BBSR for hosting me ifor the duration of this project, as well as to Indian Academy of Sciences for giving me the opportunity to work under my guide. I would also thank my fellow summer interns at IOP, BBSR for occasionally reviving me out of boredom. I would always be indebted to my family members for constant moral support.

References

[1] Mermin, N. D., 1979,*"The topological theory of defects in ordered media"*, Rev. Mod. Phys.51, 591 (1979).

[2] Patankar S., 2008,*"Order parameter spaces with point group symmetry"*, Prayas Vol. 3, No.6, Nov.-Dec. (2008)

Machine Learning Applied to Multi-Electron Events in Scintillator

Harrison LaBollita[1,3] *[*]**Morten Hjorth - Jensen**[2,3] **Sean Liddick**[3]
[1]Class of 2019, Department of Mathematics and Physics, Piedmont College, Demorest, GA
[2]National Superconducting Cyclotron Laboratory, East Lansing, MI
[3]Department of Physics and Astronomy, Michigan State University, East Lansing, MI

Abstract. Conversion electron spectroscopy is a viable tool when studying the nuclear phenomenon, shape coexistence. When a neutron-rich nucleus beta decays, a neutron transforms into a proton and emits an electron (β). The excited nucleus can then interact electromagnetically with the surrounding orbital electrons. This can result in the ejection of an electron (e^-) from the atom, a process called internal conversion. Because this process is essentially simultaneous in time, it is pivotal to differentiate between the electron (β) emitted from the nucleus and the internal conversion electron (e^-) emitted from the atom. Here we apply supervised machine learning algorithms to distinguish between one and two electron events, as well as determine the origin of the electron. We used two different convolutional neural network (CNN) architectures to accomplish these tasks. With simulated data, we were able to successfully train a CNN to distinguish between a one and two electron event with 96.79% accuracy. Furthermore, we successfully trained a CNN to predict the origin of the electron for one electron events. Our results show promise that our models' performance will generalize to experimental data. Once our models are complete, machine learning will be an important data analysis tool for conversion electron spectroscopy.
Keywords: Nuclear shape coexistance, Machine learning, Neural networks.

1. INTRODUCTION

The classical picture of spherical nuclei is far from the reality of the true nuclear structure. Shape coexistence is a nuclear phenomenon, where the nucleus exists in two stable shapes at the same excitation energy [1]. Nuclear properties, such as shape coexistence, are expected to vary significantly as a function of proton and neutron number (Z,N). Their properties provide unique information on the impetuses that foster changes to the nuclear structure of rare isotopes. In some neutron-rich nuclei, 0^+ states are predicted to exhibit shape coexistence (see Fig. 1). Therefore they are compelling to study, but experimentally challenging. At low energies, where the only energetically allowed decay mode is $0^+ \rightarrow 0^+$, conversion electron spectroscopy is the only viable technique to probe their properties. These shape-coexisting states are paramount in understanding changes to the nuclear structure of exotic nuclei (see below for further discussion) [2].

*hlabollita0219@lions.piedmont.edu

Radioactive nuclei are produced and isolated at the National Superconducting Cyclotron Laboratory (NSCL) at Michigan State University. Sean Liddick's group focuses on characterizing transition rates of ground and excited states in nuclei as a function of proton and neutron number. The decay transition rates of the excited states can provide quintessential information of the coexisting structures. Sean Liddick's group employs conversion electron spectroscopy to study these transition rates. When a neutron-rich nucleus beta decays, a neutron transforms into a proton and emits an electron (β). The excited nucleus can then interact electromagnetically with the surrounding orbital electrons. This can result in the ejection of an internal conversion electron (e^-) from the atom [3]. Because this process is essentially simultaneous in time, it is pivotal to differentiate between the electron (β) emitted from the nucleus and the internal conversion electron (e^-) emitted from the atom.

Machine learning may offer a means to a solution for this problem. A sub-field of artificial intelligence, machine learning is becoming ubiquitous in all fields of science. Due to the current information revolution, there has been an exponential increase in computational power. With this ability to effectively and efficiently apply new techniques to large datasets, machine learning has been blossoming [4]. Many researchers are finding it advantageous to employ these techniques to their own data analysis. Sean Liddick's group records a substantial amount of data making their experiment a potential candidate for machine learning techniques. In this paper, we attempt to use supervised machine learning techniques as a means to distinguish between one (e^-) and two (β, e^-) electron events and predict the electron's initial positions based on the energy depositions in a scintillator.

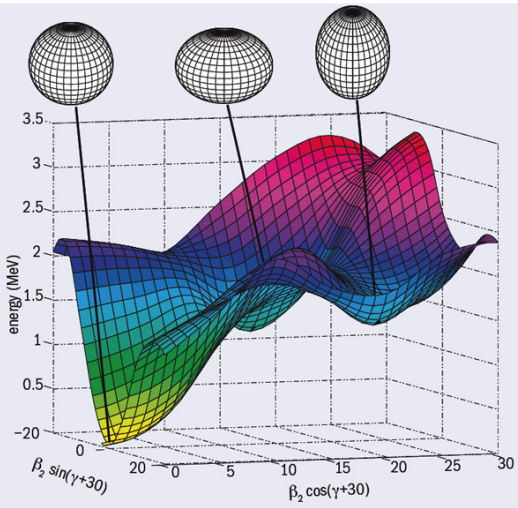

Figure 1. Shape coexistence is a nuclear phenomenon can have nuclei exist in variety of shapes at similar energies. An example of this is ^{186}Pb [5].

2. ELECTRON EVENTS

In this experiment, a scintillator with dimensions 4.8 cm $\times$ 4.8 cm $\times$ 0.3 cm is divided into a 16 $\times$ 16 grid, with a total of 256 grid sites. Each grid site or pixel on the detector is 3 mm $\times$ 3 mm. For a given event, the energy deposited in each pixel is recorded.

The data sets that we are using to implement our machine learning techniques were simulated by Sean Liddick. The simulation consists of a detector that is a single crystal of $CeBr_3$. Two different data sets were created. For the first simulated data set, the source was a single 3.06 MeV electron emitted isotropically with a starting position distributed uniformly throughout a rectangular volume of size 3 cm $\times$ 3 cm $\times$ 0.3 cm centered on the detector itself. For the second data set, the source was two 3.06 MeV electrons emitted independently in the same isotropic manner as the single electron case. Note that this simulation does not consider the simultaneous emission of these two electrons. During the electron scattering process, it is possible for the electron(s) to deposit energy in multiple locations, however these locations will always be contiguous. It is important to note that the simulation contains no light emission and no energy resolution. Figure 2 is a visual representation of the two different types of electron events.

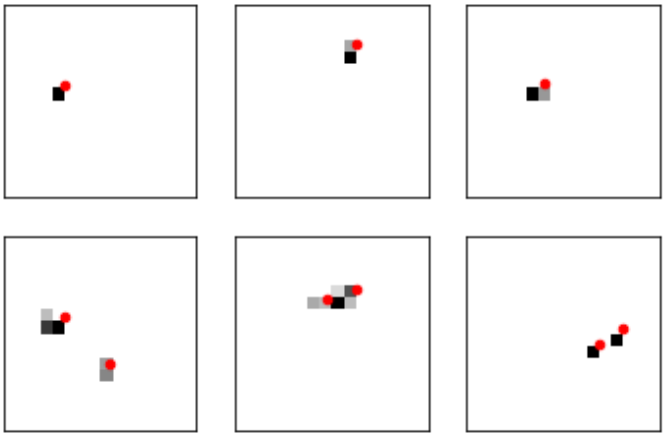

Figure 2. Top: One electron events. Bottom: Two electron events. Red dots indicate the starting position(s) of the electron(s).

The goal is to implement machine learning techniques to distinguish between a one electron event, where there is a single contiguous interaction site and a two electron event, where there can be multiple contiguous interaction sites or a larger contiguous interaction site compared to the single electron case. In addition, we will identify the initial position (x_0, y_0) of the electron(s) for an event.

3. CONVULATIONAL NEURAL NETWORK

We chose to use convolutional neural networks as a means to perform our desired tasks. Convolutional neural networks (CNN) are a class of deep neural networks optimized for analyzing images. CNNs provide the computer with the ability to see. This will allow us to treat each scintillator event as a visual image, so the computer can see the electron's interaction sites on the scintillator. For a detailed explanation on convoluational neural networks and other machine learning techniques, see [4]. The source code for these two CNNs are located at this link.

3.1 *Single-Electron Model*

We created a CNN architecture in Keras[1] to predict the origin of the electron in single-electron events. We first created two mutually exclusive sets from the single-electron data set. Our training set consisted of 333,333 events and our testing set consisted of 20,000 events. Our CNN architecture consisted of one two-dimensional convolutional layer, where the output from this layer was then flattened into a one dimensional array and connected to a feed forward neural network layer with 512 nodes. This layer was connected to the output layer with two nodes, which are representative of the x and y positions of the electron. We used the following loss function

$$\text{MSE} = \frac{1}{N}\sum_{i=0}^{N-1}(\hat{y}_i - y_i)^2. \tag{1}$$

Figure 3 shows the model's performance throughout the duration of the training. After training the model for ten epochs, we achieved a model accuracy of 96%.

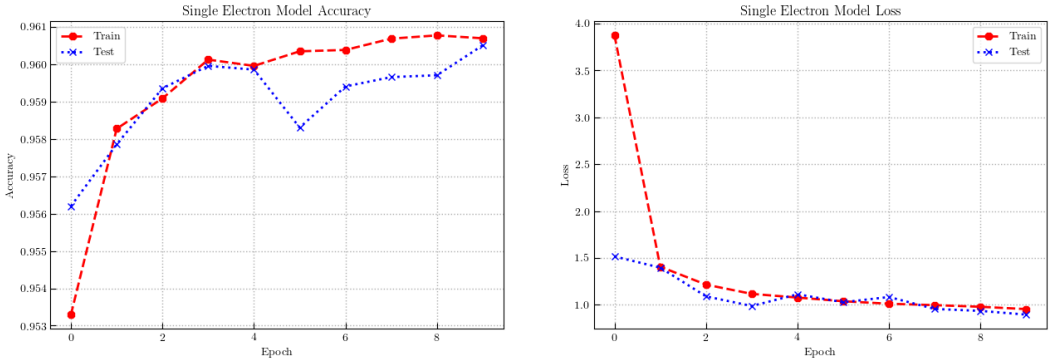

Figure 3. Single-Electron Model was trained for ten epochs. Left: Model's accuracy after each epoch. Right: Model's loss after each epoch.

[1] https://keras.io

3.2 *Multi-Electron Model*

The second CNN architecture was designed to correctly categorize a one and two-electron event. Firstly, we created a new data set that contained both one and two-electron events. This was done by randomly selecting events from each data set until our new data set had size 200,000. We then trained the CNN on 150,000 events and tested on the remaining 50,000 events.

Our CNN architecture consisted of two two-dimensional convolutional layers that were then connected to a two-dimensional max pooling layer. This was then connected to a single neural network layer with 128 nodes. Finally, this was connected to the output layer, which was another neural network layer with two nodes, where one node represents the probability of the event being a one-electron event and the other represents the probability of a two-electron event. We used the categorical cross entropy loss function for training our model. This loss function has the form

$$H(y) = -\sum_i y_i \log(\hat{y}_i), \tag{2}$$

where $\hat{y}_i$ is the predicted probability of the event being class i and y_i is the true probability of the event bein class i.

4. RESULTS

4.1 *Single Electron Model*

The Single-Electron Model was designed to predict the origins of the electron in one-electron events. After training, our model was 96% accurate on the testing set. When evaluating the distances between the predicted value $(\hat{x}, \hat{y})$ and the actual value (x_0, y_0), we found that on average our model predicted points about 1.2 mm away from the actual origin. This is promising considering the width of a pixel totals in 3 mm, so the majority of the time we are predicting points that are within the same pixel. However, to further benchmark the performance of our model, we compared it with a random guessing algorithm. Using the assumption that the electron starts in the pixel with the highest energy (which is correct 70% of the time), the algorithm was written to randomly pick a point within that pixel. Figure 4 shows a comparison of the CNN predictions to the random guessing algorithm predictions. The histogram plots show the distance between the predicted ($\hat{x}$, $\hat{y}$) and the actual (x, y) on the x-axis and then the frequency of these distances on the y-axis.

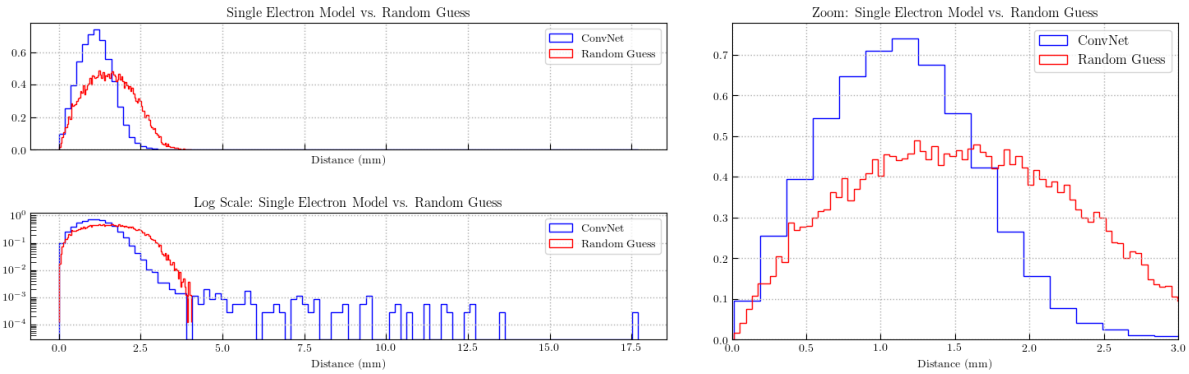

Figure 4. On the left are two plots representing the Single-Electron Model's predictive error versus the error of the random guessing algorithm. On the right limits the x-axis to [0,3].

On average, the random guessing algorithm predicted points that were 1.5 mm away from the actual point. Our model's error was less than the random guessing algorithm's on average 77% of the time. This means our model's performance is better the majority of the time than randomly guessing. However, our neural network's prediction is still only marginally better than the random guess. Therefore, it is necessary to define a proper uncertainty quantification and resolution scale so that a true benchmark for our neural network's performance can be conducted. Table 1 contains more metrics from the Single-Electron Model's performance and the random guessing algorithm's performance. The table includes the average distance between the actual origin and the predicted origin of the electron, the closest prediction to the actual origin of electron, the furthest prediction from the actual origin of electron, and the 90^{th}, 95^{th}, 99^{th} percentiles. The percentiles show that 90%, 95%, and 99% of our predictions were 1.9 mm, 2.165 mm, and 3.293 mm from the actual origin of the electrons, respectively.

Table 1. Metrics for Single-Electron Model and Random Guessing Algorithm (mm)

Method	**Average**	**Min**	**Max**	**90 %**	**95 %**	**99 %**
Single Electron Model	1.2117	0.011	21.253	1.900	2.165	3.293
Random Guessing	1.555	0.008	3.944	2.574	2.805	3.218

4.2 *Multi-Electron Model*

The Multi-Electron Model was designed to distinguish between a one-electron and two-electron event given only the scintillator with the amount of energy deposited in each pixel. After training, our model achieved a 96.79% accuracy (see Figure 5). This means the model was able to successfully distinguish the difference between the simulated one and two-electron events. This result

shows promise of our CNN model's generalizability to real experimental data.

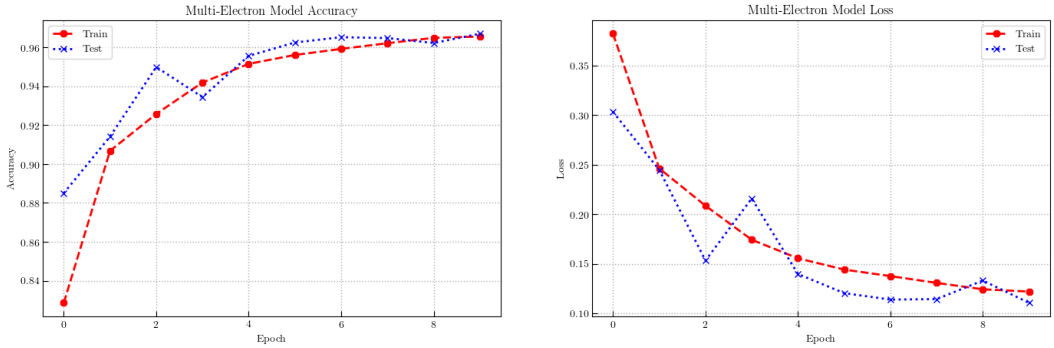

Figure 5. The Multi-Electron model was trained for ten epochs. Left: Model's accuracy of the model after each epoch. Right: Model's loss of the model after each epoch.

5. CONCLUSION

With the implementation of machine learning techniques, we were able to successfully train a CNN to distinguish between a one and two-electron event. Furthermore, we successfully trained a CNN to predict the origin of the electron for one-electron events. Relative to the size of a pixel, our model's mean error was marginally better than that of the random guessing algorithm's, therefore a proper uncertainty quantification needs to be explored. This technique will be generalized to predict the origins of the electrons in the two-electron case and their respective initial energies. These models were trained and tested on simulated data provided by Sean Liddick, so they will need to be tested with a data set with light emission and an energy resolution. Once these models are completely generalized, they can then be applied to real experimental data. If they perform well on the experimental data, then machine learning will be a viable data analysis technique for the Sean Liddick group and conversion electron spectroscopy in general.

6. ACKNOWLEDGMENTS

This work would not have been possible with out the help of Nicholas Todoroff, Jane Kim, Yani Udiani, and Robert Branson.Thank you Morten for allowing me to work alongside you and your team. Thank you Sean for allowing us to work with you on exploring new data analysis techniques for your experiment.

References

[1] R. Lucas. Nuclear shapes. Europhys. News, (2001)

[2] A. Gade and S.N. Liddick. Journal of Physics G: Nuclear and Particle Physics, 43(2), 1 (2016)

[3] O. Dragoun. Internal Conversion-Electron Spectroscopy. *Advances in Electronics and Electron Physics*, Vol 60. Academic Press, 1983. doi:https://doi.org/10.1016/S0065-2539(08)60888-4. URL http://www.sciencedirect.com/science/article/pii/S0065253908608884

[4] P. Mehta, M. Bukov, C. H. Wang, A. G. R. Day, C. Richardson, C. K. Fisher and D. J. Schwab. ArXiv: 1803.08823.

[5] Andrei Andreyev and K U Leuven and Jürgen Kluge. *Exotic lead nuclei get into shape at ISOLDE* CERN Courier, 19 Sept 2007

Real Space Renormalization Group for One-Dimensional Ising Chains

Shraddha Singh[1] **and Vijay Singh**[2**]
[1]Int. M.Sc Student, 2014-19 Batch, Department of Physics, UM-DAE, Centre for Excellence in Basic Sciences, Mumbai University, Kalina, Santa-Cruz East, Mumbai 400 098, India.
[2]Department of Physics, UM-DAE, Centre for Excellence in Basic Sciences, Mumbai University, Kalina, Santa-ruz East, Mumbai 400 098, India.

Abstract. We apply the real space Renormalisation Group (RNG) technique to a variety of one-dimensional Ising chains. We begin by recapitulating the work of Nauenberg for an ordered Ising chain, namely the decimation approach. We extend this work to certain non-trivial situation namely, the Alternate Ising Chain and Fibonacci Ising chain. Our approach is pedagogical and accessible to undergraduate students who have had a first course in statistical mechanics.
Keywords: Renormalisation group, Ising chains.

1. INTRODUCTION

There is a deep and useful connection between Statistical Mechanics and Quantum Field Theory. Kenneth Wilson appreciated this connection and applied the renormalization ideas to statistical mechanics[1]. Application of these techniques to both classical and quantum many body problems have seen success. However, RNG calculations are often very complex and the approximations made are sometimes obscure. Often, one has to resort to extensive numerical calculations.

The present work is written in the spirit of conveying some essential ideas of RNG to a beginner and applying this approach to more complicated Ising chains. We present some pedagogical examples of a form of real space RNG termed Decimation. This technique was introduced by Michael Nauenberg in the context of the one-dimensional Ising model. Unfortunately, this attractive piece of work [2] is marked by several typographical errors. We present Nauenberg's work in a simplified (and hopefully error-free) fashion. We extend it to related Hamiltonians such as the Alternate Ising model and Fibonacci chain Ising model.

The RNG strategy can be symbolically stated as follows. It transforms the Hamiltonian, e.g. $H^{'} = \mathbb{R}(H)$. Next, one iterates it, $H^{''} = \mathbb{R}(H')$ until one obtains a fixed point Hamiltonian, $H^{*} = \mathbb{R}(H^{*})$. The flow towards the fixed point Hamiltonian and the Hamiltonian H^{*} itself yields insight into the physical properties of the system. Wilson suggested such a procedure and was able to elicit the critical properties of the 2D and the 3D Ising model and a famous quantum system namely, the Kondo problem[3].

**physics.sutra@gmail.com

In Sec. 2, we recapitulate the work of Nauenberg and describe how decimation is carried out for the one-dimensional Ising model. In Sec. 3, we extend this approach to alternate Ising model where the coupling is alternate like in a binary alloy. In Sec. 4, we discuss the Fibonacci Ising chain. Sec. 5 constitutes the conclusion.

2. ONE DIMENSIONAL ISING MODEL

We start with the familiar one-dimensional Ising model for N spins, $S_i = \pm 1$, $i = 1, 2...N$, with nearest neighbour coupling constant J, see Fig.(1).
The Hamiltonian H_N for this model is written as,

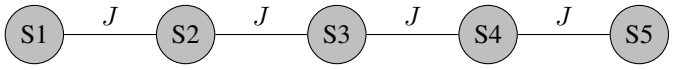

Figure 1.: One Dimensional Ising Spin model

$$H_N = -\frac{J}{kT}\sum_{i=1}^{N} S_i S_{i+1}, \text{ where } S_{N+1} = S_1 \tag{1}$$

One can consider the dimensionless Hamiltonian H_N, without loss of generality,

$$H_N(K) = -K\sum_{i=1}^{N} S_i S_{i+1} \qquad (\frac{J}{kT} = K) \tag{2}$$

Note that $K > 0$ implies ferromagnetism.

2.1 *Decimation*

Let $\mathbb{P}$ be the transfer matrix such that $\mathbb{P}(i, i+1) = \exp(KS_iS_{i+1})$. Thus,

$$Z_N = \sum_{s_1, s_2, s_3 ...} exp(-H_N(K)) = \sum \mathbb{P}(S_1S_2)\mathbb{P}(S_2S_3)\mathbb{P}(S_3S_4)... \tag{3}$$

$$\mathbb{P} = \begin{bmatrix} e^K & e^{-K} \\ e^{-K} & e^K \end{bmatrix} \tag{4}$$

As the elements of the matrix depend on the product S_iS_{i+1} which is same for all i, we can write

$$Z_N = \sum_{s_1, s_2, s_3 ...} (\mathbb{P}(\mathbb{K})^N) = Tr(\mathbb{P}(\mathbb{K})^N) \tag{5}$$

Now, instead of computing the usual partition sum as shown above, we consider only the partial sum of $exp[-H_N(K)]$ over all possible values of even spins, $S_i = \pm 1, i = 2, 4, ...$ and for even N we obtain a scaled partition function $exp[-H_N(K')]$, (see Fig. (2)).

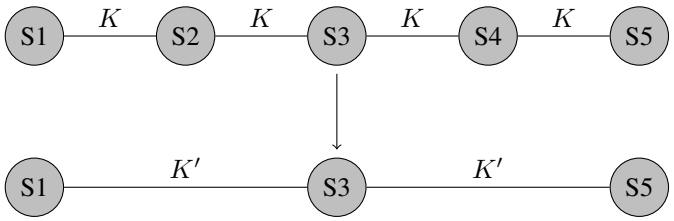

Figure 2.: Decimation

The Hamiltonian becomes,

$$\sum_{[s_2 s_4 .. s_N]} exp[-H_N(K)] = \mathbb{P}^2_{S_1 S_3} \mathbb{P}^2_{S_3 S_5} .... \mathbb{P}^2_{S_{N-1} S_1} \tag{6}$$

The idea behind this partial summation is to find a renormalization transformation K$\rightarrow$ $K^{'}$ such that,

$$\mathbb{P}^2(K) = exp[2g(K)]\mathbb{P}(K^{'}) \tag{7}$$

$$\sum exp(-H_N(K)) = Tr\mathbb{P}(\mathbb{K})^N = Tr[\mathbb{P}(\mathbb{K})^2]^{\frac{N}{2}}, \tag{8}$$

where g(K) is a scalar function of K. Then $K^{'}$ can be interpreted as an effective Ising coupling constant for the remaining odd spins $S_i, i = 1, 3, 5....N-1$ and Eq. (8) may (formally) be written as.

$$exp(-H_N(K)) = \mathbb{P}(\mathbb{K})^N \tag{9}$$

$$= [exp(2g(K))\mathbb{P}(\mathbb{K}')]^{N/2} \tag{10}$$

$$= exp(Ng(K))[(\mathbb{P}(K'))]^{N/2} \tag{11}$$

$$= exp(Ng(K))exp(-H_{\frac{N}{2}}(K')) \tag{12}$$

Thus, the resulting equation becomes,

$$\sum_{[s_1 s_2 .. s_N]} exp[-H_N(K)] = \sum_{[s_1 s_3 .. s_N]} exp[-H_{N/2}(K^{'}) + Ng(K)] \tag{13}$$

To make the procedure clear we discuss the case of 3 spins,

$$e^{K' S_1 S_3} * e^{2g(K)} = \sum_{S_2=+1}^{-1} e^{K S_1 S_2} * e^{K S_2 S_3} \tag{14}$$

$$= e^{K(S_1+S_3)} + e^{-K(S_1+S_3)} \tag{15}$$

If $S_1 = S_3 = +1$

$$e^{K'} * e^{2g(K)} = e^{2K} + e^{-2K} \tag{16}$$

If $S_1 = -S_3 = +1$

$$e^{-K'} * e^{2g(K)} = 2 \tag{17}$$

Using Eq.(17) we obtain g(K)

$$g(K) = \frac{1}{2}K^{'} + \frac{1}{2}\text{ln2} \tag{18}$$

Next using Eq. (16) we obtain K'

$$K^{'} = \frac{1}{2}\text{ln}\{\text{cosh(2K)}\} \tag{19}$$

Thus K' is defined by a non-linear transformation. We denote this as $K' = f(K)$. Near the fixed point $K' = K^* + \epsilon$,

$$K' = f(K^* + \epsilon) \tag{20}$$

$$K^* + \epsilon' = f(K^*) + \epsilon f'(K^*) \tag{21}$$

As $K^* = f(K^*)$ near a fixed point K* we have

$$\epsilon' = \epsilon f'(K^*) \tag{22}$$

which is a linear transformation that resembles

$$\epsilon' = \lambda\epsilon \tag{23}$$

where $\lambda = \tanh(K^*)$.

There are two fixed points for the equation $K^* = \ln\{\cosh(2K^*)\}/2$, 0 and ∞ with $\lambda = 0$ and $\lambda = 1$ respectively. For phase transition λ must be greater than unity. This proves the well established result that there is no phase transition for 1D Ising spin model. There is another way to see this. After applying the renormalization transformation n times, the mapping $K^{n-1} \rightarrow K^{(n)}$ can be obtained from the recurrence relation,

$$K^{(n)} = \frac{1}{2}\ \text{ln}\ \{\text{cosh(2K}^{(n-1)})\} \tag{24}$$

where $K^{(0)} = K$.

$$\text{Let } \zeta = \text{tanh(K)} \tag{25}$$

$$\text{therefore } K' = \frac{1}{2}\ln\left(\frac{1+\zeta^2}{1-\zeta^2}\right) \tag{26}$$

$$\text{Hence, } \zeta' = \text{tanh(K')} = \tanh\left\{\frac{1}{2}\ln\left(\frac{1+\zeta^2}{1-\zeta^2}\right)\right\} \tag{27}$$

$$= \frac{\exp\Big(\frac{1}{2}\ln\Big(\frac{1+\zeta^2}{1-\zeta^2}\Big)\Big) - \exp\Big(-\Big(\frac{1}{2}\ln\Big(\frac{1+\zeta^2}{1-\zeta^2}\Big)\Big)\Big)}{\exp\Big(\frac{1}{2}\ln\Big(\frac{1+\zeta^2}{1-\zeta^2}\Big)\Big) + \exp\Big(-\Big(\frac{1}{2}\ln\Big(\frac{1+\zeta^2}{1-\zeta^2}\Big)\Big)\Big)} \tag{28}$$

$$= \frac{\sqrt{\frac{1+\zeta^2}{1-\zeta^2}} - \sqrt{\frac{1-\zeta^2}{1+\zeta^2}}}{\sqrt{\frac{1+\zeta^2}{1-\zeta^2}} + \sqrt{\frac{1-\zeta^2}{1+\zeta^2}}} \tag{29}$$

$$= \frac{(1+\zeta^2)-(1-\zeta^2)}{(1+\zeta^2)+(1-\zeta^2)} \tag{30}$$

Thus,

$$\zeta' = \zeta^2 \tag{31}$$

$$\text{tanh(K')} = \text{tanh(K)}^2 \tag{32}$$

Since tanh(K) < 1, tanh(K^n) tends to zero as $n \longrightarrow \infty$. This suggests that the coupling gets weaker with each decimation and we are left with a non-itneracting system which will show no phase transition. We next discuss the more complex (unequal J_i) one-dimensional Ising models.

3. ALTERNATE ISING MODEL

Here the $K_i's$ are arrranged in the manner shown in Fig.(3).

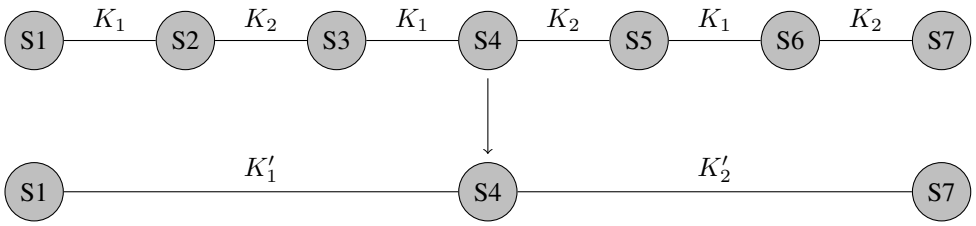

Figure 3.: Similar Decimation for Alternate Ising Model

In order to adopt a similar decimation procedure we need to consider four spins at a time. This is

illustrated in Fig.(3). Using this procedure,

$$e^{K_1' S_1 S_4} * e^{g_1} = \sum_{S_2,S_3} e^{K_1 S_1 S_2} * e^{K_2 S_2 S_3} * e^{K_1 S_3 S_4} \tag{33}$$

$$= \sum_{S_3} e^{K_1 S_3 S_4} * 2\text{cosh}(K_1 S_1 + K_2 S_3) \tag{34}$$

$$= e^{K_1 S_4} * 2cosh(K_1 S_1 + K_2) + e^{-K_1 S_4} * 2\text{cosh}(K_1 S_1 - K_2) \tag{35}$$

Like in the previous section, we consider $S_1 = S_4 = +1$ to obtain ,

$$e^{K_1'} * e^{g_1} = e^{K_1} * 2\text{cosh}(K_1 + K_2) + e^{-K_1} * 2\text{cosh}(K_1 - K_2) \tag{36}$$

and $S_1 = -S_4 = +1$ to obtain,

$$e^{-K_1'} * e^{g_1} = e^{-K_1} * 2\text{cosh}(K_1 + K_2) + e^{K_1} * 2\text{cosh}(K_1 - K_2) \tag{37}$$

Using Eqs.(36) and (37), and cosh(x)=cosh(-x) we obtain,

$$e^{2K_1'} = \frac{e^{K_1}\text{cosh}(K_1 + K_2) + e^{-K_1}\text{cosh}(K_1 - K_2)}{e^{K_1}\text{cosh}(K_1 - K_2) + e^{-K_1}\text{cosh}(K_1 + K_2)} \tag{38}$$

employing the addition properties of cosh function, we obtain,

$$\text{tanh}(K_1') = \text{tanh}^2(K_1)\text{tanh}(K_2) \tag{39}$$

One similarly obtains,

$$\text{tanh}(K_2') = \text{tanh}^2(K_2)\text{tanh}(K_1) \tag{40}$$

The fixed points are,$\{K_1^*, K_2^*\} = \{0, 0\}$ or $\{\infty, \infty\}$.

Note that we need to block spins in a judicious way. If we block them in a non similar fashion, i.e. if the new lattice is not alternate (see Fig.(4)), then,

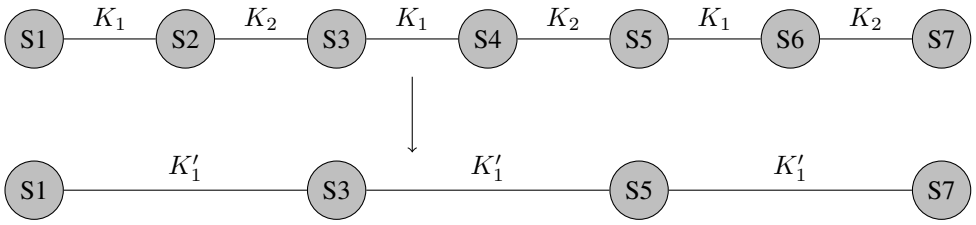

Figure 4.: Non similar decimation

$$\text{tanh}(K_1') = \text{tanh}(K_1)\text{tanh}(K_2) \tag{41}$$

In this case a fixed point discussion is not possible as K_2' does not exist. However, the free energy is conserved in either case.

4. FIBONACCI CHAIN ISING MODEL

In this section we consider a fibonacci series where two $b's$ are never adjacent $i.e.$ the nearest neighbour of 'b' is always 'a' (see Fig.(5)). We suggest a method to generate the decimation procedure below.

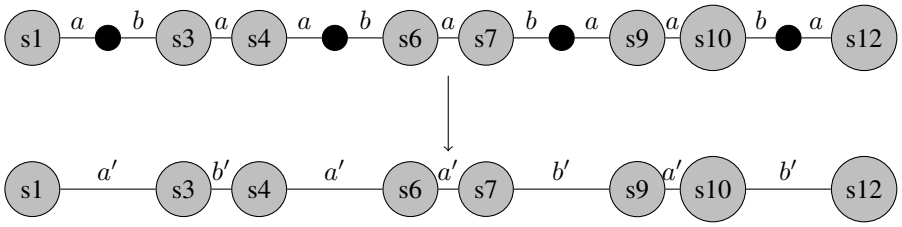

Figure 5.: Blocking in the Fibonacci Ising model

4.1 *Matrix method for generation*

It is well know that the Fiboanacci chain can be generated by setting up a number of rules for rabbit procreation. In the present case we generate it by the mathematical operation shown below.

$$M = \begin{bmatrix} 1 & 1 \\ 1 & 0 \end{bmatrix}, \quad N^{(0)} = \begin{bmatrix} N^{(0)_A} \\ N^{(0)_B} \end{bmatrix} = \begin{bmatrix} A \\ B \end{bmatrix} : AB \tag{42}$$

$$MN^{(0)} = \begin{bmatrix} 1 & 1 \\ 1 & 0 \end{bmatrix} \begin{bmatrix} A \\ B \end{bmatrix} = \begin{bmatrix} A+B \\ A \end{bmatrix} : ABA = N^{(1)} \tag{43}$$

$$MN^{(1)} = \begin{bmatrix} 1 & 1 \\ 1 & 0 \end{bmatrix} \begin{bmatrix} A+B \\ A \end{bmatrix} = \begin{bmatrix} A+B+A \\ A+B \end{bmatrix} = \begin{bmatrix} N^{(2)_A} \\ N^{(2)_B} \end{bmatrix} = N^{(2)} : ABAAB \tag{44}$$

$$MN^{(2)} = \begin{bmatrix} 1 & 1 \\ 1 & 0 \end{bmatrix} \begin{bmatrix} A+B+A \\ A+B \end{bmatrix} = \begin{bmatrix} A+B+A+A+B \\ A+B+A \end{bmatrix} = \begin{bmatrix} N^{(3)_A} \\ N^{(3)_B} \end{bmatrix} = N^{(3)} : ABAABABA \tag{45}$$

and so on.

For general iteration,

$$N_A^{(n+1)} = M_{11}N_A^{(n)} + M_{21}N_B^{(n)} \quad M_{11} = M_{21} = M_{12} = 1 \tag{46}$$

$$N_B^{(n+1)} = M_{12}N_A^{(n)} + M_{22}N_B^{(n)} \quad M_{22} = 0 \tag{47}$$

as $n \longrightarrow \infty$, the ratio $r = \lim_{n\longrightarrow\infty} N^{(n)_A}/N^{(n)_B} \longrightarrow (\sqrt{5}+1)/2$. Here N_A, N_B are length scales of bond A and B respectively.

4.2 *Decimation method*

Consider now the Ising Chain shown in Fig.(6):

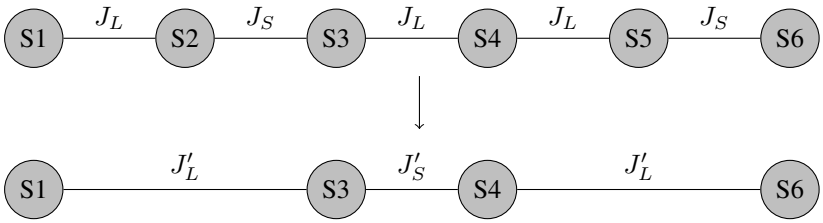

Figure 6.: Self-similar blocking for Fibonacci chain

Let $K_i = J_i/kT$

$$H_N(K) = -\sum_{i=1}^{N-1} K_i S_i S_{i+1} \tag{48}$$

$$e^{K'_L S_1 S_3} * e^{g_1} = \sum_{S_2=+1}^{-1} e^{K_L S_1 S_2} * e^{K_S S_2 S_3} \tag{49}$$

As in the previous sections, let $S_1 = S_3 = +1$ we obtain,

$$e^{K'_L} * e^{2g_1} = e^{K_L+K_S} + e^{-(K_L+K_S)} \tag{50}$$

and $S_1 = -S_3 = +1$ yields,

$$e^{-K'_L} * e^{2g_1} = e^{K_L-K_S} + e^{-(K_L-K_S)} \tag{51}$$

Using Eqs.(50) and (51), and $cosh(x) = cosh(-x)$ leads to,

$$tanh(K'_L) = tanh(K_L)tanh(K_S) \tag{52}$$

$$\text{and } g_1 = \frac{1}{2}K'_L + \frac{1}{2}ln(2cosh(K_L - K_S)) \tag{53}$$

For the ordered case ($K_L = K_S$) the tansformation reduces to $tanh(K') = tanh^2(K)$ and g_1 is given by the same expression as Eq.(18). Further, $K'_S = K_L$ and $g_2 = 0$. Hence, all the above equations are consistent with ordered case. The fixed points in this case are,$\{K_1^*, K_2^*\} = \{0, 0\}$ or $\{\infty, \infty\}$.

Self similarity is preserved if the new lengths follow the following relation.

$$\frac{L'}{S'} = \frac{L}{S} \tag{54}$$

But $L' = L + S$ and $S' = L$. Thus,

$$1 + \frac{S}{L} = \frac{L}{S} = x \tag{55}$$

$$1 + \frac{1}{x} = x \tag{56}$$

which leads to $x = (\sqrt{5}+1)/2$, the golden ratio.

5. CONCLUSION

This decimation approach is perhaps the simplest version of RNG. Its extension to higher dimension however gets tricky. The solution to this problem uses the Migdal Kadanoff transformation[4],[5]. Interestingly, this decimation procedure inspired similar work in quantum systems. We hope to describe this quantum version introduced by Bhat, Singh and Subbarao[6] in the future.

6. ACKNOWLEDGMENT

One of us (VAS) acknowledges support from the Raja Ramanna Fellowship by the DAE.

References

[1] Wilson K.G., Phys. Rev. B **4**, 1374 (1971).
[2] Nauenberg M., J. Math. Phys. **16**, 703 (1975).
[3] Wilson K.G., Rev. Mod. Phys. **47** , 773 (1975).
[4] Kadanoff L.P., Ann. Phys. (N.Y.) **100**, 359 (1976).
[5] Migdal A.A., Soy. Phys. JETP **42**, 743 (1976).
[6] Bhat G.R. Singh V.A. and Subbarao K., J. Phys. C, Solid State Physics, **17**, 5569 (1984).

Software Development to Determine the Optimal Parameters of a Tape Transport System

A. Torode[1,2,3]*, M. K. Smith[1,3], A. Spyrou[1,2,3], C. Harris[1,2,3], S. Lyons[1,3], A. C. Dombos[1,2,3], S. N. Liddick[1,4]

[1] 5th year senior, National Superconducting Cyclotron Laboratory, Michigan State University, East Lansing, Michigan 48824, USA
[2]Department of Physics and Astronomy, Michigan State University, East Lansing, Michigan 48824, USA
[3]Joint Institute for Nuclear Astrophysics, Michigan State University, East Lansing, Michigan 48824, USA
[4]Department of Chemistry, Michigan State University, East Lansing, Michigan 48824, USA

Abstract. To better understand the process of nucleosynthesis in stars today, advanced nuclear physics techniques are needed. At the National Superconducting Cyclotron Laboratory, at Michigan State University, a new tape transport system has been developed for this purpose. Radioactive nuclei can be implanted on the tape system, and after detecting the products of their decay, the tape rotates to remove any remaining unwanted activity. The present work focuses on the development of software to be used for calculating the optimum settings for experiments using the tape transport system.
Keywords: Nucleosysthesis, Radioactivity

1. INTRODUCTION

All of the heavy elements that exist on earth today were formed inside stars through various nuclear reactions and processes. The process of creating elements heavier than hydrogen is referred to as nucleosynthesis. Ever since this process was first described [1], the understanding of stellar nucleosynthesis has advanced significantly. It is currently believed that hydrogen and helium were created during the Big Bang [2] and then the abundance of heavier elements up to iron are created through nuclear reactions inside of stars [1]. The elements heavier than iron are created with different processes, which are termed the s-process, p-process, and r-process [1]. The s-process is a slow process where neutrons are captured and γ radiation is emitted, abbreviated as (n, γ), followed by β decays [1]. The p-process, also known as the γ-process involves the γ-excitation of nuclei followed by the emission of charged particles and neutrons [4]. The r-process is a rapid process of neutron capture reactions followed by β decays.

The r-process is believed to be responsible for producing nearly half of the heavy elements found in nature [5]. Neutron capture rates, β-decay rates, and β-delayed neutron emission probabilities are three important quantities that go into performing r-process nucleosynthesis calculations

*awtorode@gmail.com

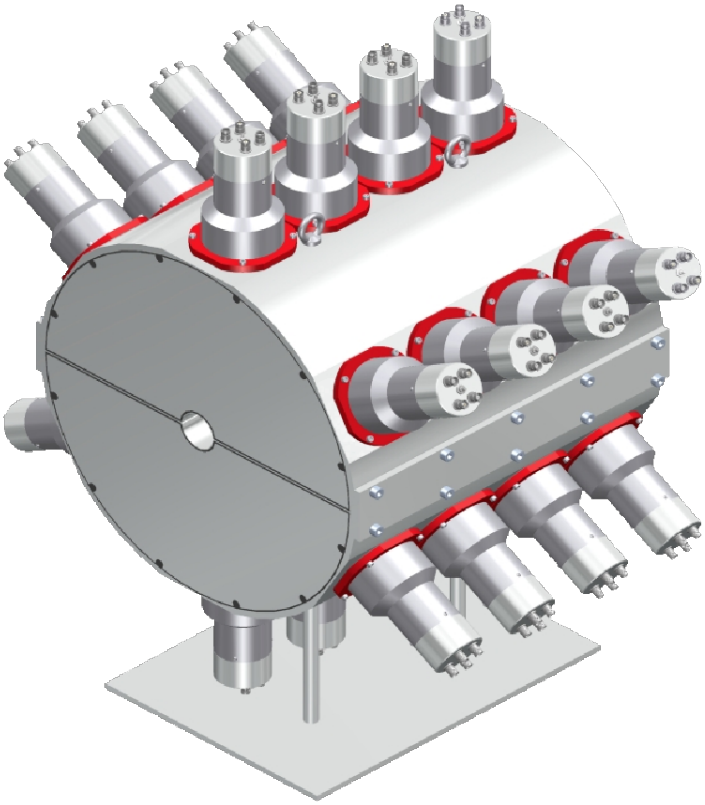

Figure 1. The SuN (Summing NaI(Tl)) detector.

[5]. Therefore in order to better understand the nucleosynthesis of heavy elements, advanced techniques are needed to measure and study decays of the exotic neutron-rich nuclei involved in the r-process and to constrain astrophysical models. For the purpose of this paper we will focus on β-decay rates. Neutron-rich isotopes can often undergo β^- decay, during which one of their neutrons is converted to a proton, and in this way transforms the original radioactive nucleus into a new one. During this process, an antineutrino and electron (β^--particle) are also emitted. This process does not change the atomic mass number of the decaying isotope, but will change the isotope itself. Once the β decay is completed, a new element will exist which may itself be unstable and β decay. This process will continue until a stable isotope is reached.

Since the process of β decay is important in understanding the r-process, many advanced techniques and detectors have been created for the purpose of understanding it. At the National Superconducting Cyclotron Laboratory (NSCL) at Michigan State University (MSU), a γ-ray calorimeter (known as SuN) was developed for this purpose [6]. The Summing NaI(Tl) (SuN) detector shown in Fig. 1 is used to study β decays in neutron-rich nuclei. This detector is a barrel shaped scintillator,

divided into eight optically isolated segments of NaI(TI). Each segment is read by three photomultiplier tubes (PMTs), for a total of 24 signals from the detector [6]. It is highly efficient and has a 45 mm bore-hole through its center for use around a beam pipe.

For isotopes with a relatively short half-life (roughly less than 1 second), an implantation-β decay correlation method with fast beams can be used [3][7]. However, this technique is not applicable if the half-life of interest is long and the total implantation rate high. For this reason, for longer half-lives it is necessary to use alternative techniques.

Neutron-rich isotopes can be far from stability with subsequent daughter isotope decays introducing unwanted background radiation. This could mean that after only a few seconds following implantation, the decays picked up by SuN could be decays from the daughter isotope instead of the mother isotope. In cases where the decaying mother isotope is of interest, this poses an issue. To reduce this background radiation, a new experimental setup was developed at the NSCL that couples the SuN detector with a tape transport system.

The premise is that after implantation onto a section of tape, the tape is moved to remove long-lived isotopes from the active volume of the SuN detector. Hence, one can reduce the issue of the daughter isotope decays becoming more prominent than the mother isotope decays. The idea of implementing a tape station has been around for over 40 years, e.g. see Ref. [9]. Since then, there have been advancements and new ideas in the way a tape station is implemented such as SATURN (Scintillator And Tape Using Radioactive Nuclei) created at Argonne National Laboratory (ANL) [10].

2. SUNTAN SYSTEM

At the NSCL, SuNTAN (SuN Tape-system for Active Nuclei) was developed (Fig. 2). The tape station consists of a main tube that fits inside of the SuN detector where tape can be fed from an isolated chamber to the end of the tube and back via motors. The entire station is vacuum sealed and the physical tape is stored in a large chamber outside of the SuN detector. A small portion of tape is exposed at the end of the tube which serves as the implantation point for a rare isotope beam inside of SuN. After a period of implantation (the duration of which is isotope dependent), the tape is moved to expose a clean section of tape to the beam and remove unwanted daughter activity.

In conjunction with SuNTAN, a new scintillating detector (Fig. 3) developed at Hope College was characterized for use with SuN. It is attached to wavelength shifting fiber optic cables to work in conjunction with the tape station for the detection of β particles. The detector utilizes two PMTs that are attached to the fiber optic cables in order to detect β decays in coincidence between one another. SuNTAN and the fiber detector will be the focus of a forthcoming publication. This publication's focus is on new software that accompanies SuNTAN and helps to guide the decision for the appropriate tape cycle.

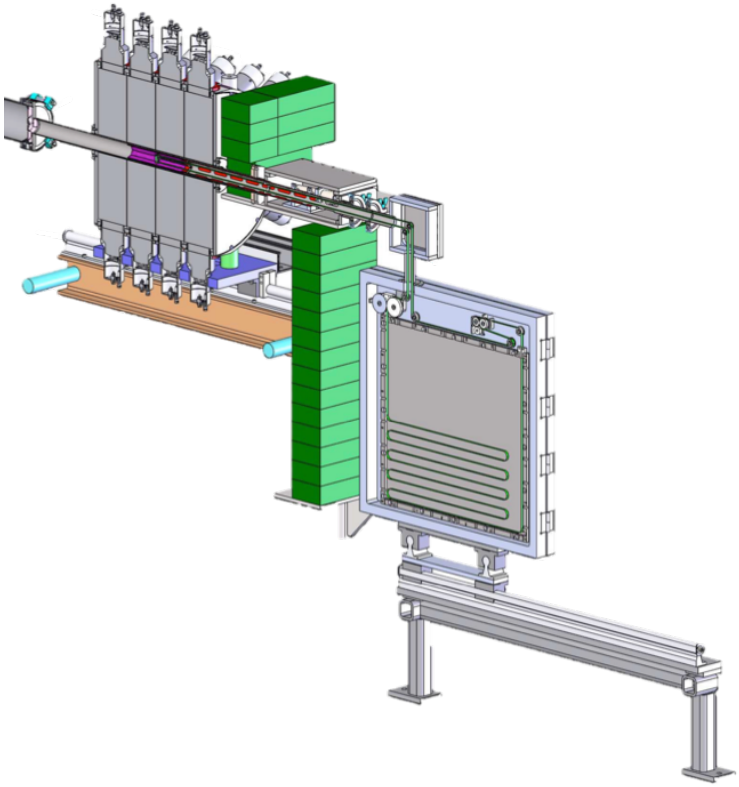

Figure 2. A cross section of the SuNTAN system connected to the SuN detector. On the bottom right is a railing system for moving the tape station into and out of SuN. Above that is the tape box where the new and used tape is located. In the top left is the SuN detector with a beam pipe going through its center. Lead bricks (green) act as a barrier to isolate the tape from within SuN.

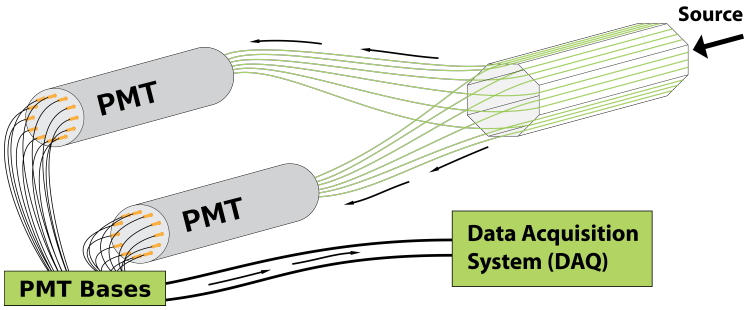

Figure 3. The scintillating detector attached to wavelength shifting fiber optic cables that carry the signal to two PMTs. After entering the PMTs the signals are recorded via the NSCL digital data acquisition system [11].

3. GINA PROGRAM

Generations of Implanted Nuclear Activity (GINA) is a program designed to work with a tape station. To demonstrate the need and functionality of GINA, the test case of ^{42}S is used. The primary isotope of ^{42}S has a half-life of $T_{1/2} = 1.03 \pm 0.03$ seconds [8]. This means that on average, half of a sample of ^{42}S will decay in that time. ^{42}S will β decay into ^{42}Cl which has a half-life $T_{1/2} = 6.8 \pm 0.3$ seconds [8]. The daughter isotope will decay to the granddaughter isotope of ^{42}Ar, having a half-life of $T_{1/2} = 32.9 \pm 1.1$ years [8]. This decay chain is perfect for the commissioning of SuNTAN due to the short half-life of the primary and daughter isotopes, and long half-life of the granddaughter.

The decay rate for an isotope is given by

$$\frac{dN(t)}{dt} = -\lambda N(t) = -\frac{N(t)}{\tau}, \tag{1}$$

where N is the number of radioactive nuclei, λ is the decay constant, τ is the mean lifetime of the particles within the material, and t is time. The decay constant is related to the half-life ($T_{1/2}$) by

$$\lambda T_{1/2} = \ln(2) \implies T_{1/2} = \tau \ln(2). \tag{2}$$

The rare isotope beam of the primary isotope will be continually implanted onto the target tape. Thus, the number of primary isotopes at the target location will continually increase as the beam is being deposited. The decay rate is directly proportional to the number of nuclei of the isotope that is present and thus the rate of decay will eventually reach equilibrium with the rate of deposition. The daughter isotope will similarly do this, but over a much longer time, due to a slower decay rate. This will cause the decay rates of the daughter isotope to slowly approach the decay rates of the primary isotope which will make it difficult to distinguish which isotope is decaying in the detectors for a given event. At the start of this cycle, the primary isotope decay rates are prominent over the daughter isotope (as there are little to no daughter nuclei present) and thus it is favorable

to collect data at this point. When it is determined that the daughter isotope is providing too much contamination, the tape of SuNTAN can be moved so the system can return to this favorable state. Two important factors to consider when running an experiment with this system are to maximize the number of primary (mother) decays and to minimize the contamination from other isotopes decaying.

In order to determine sufficient timing parameters for tape rotation, a method was established to calculate decay rates per isotope of decay chains consisting of multiple generations. The GINA program performs this method and provides various information for determining how to optimize the favorable collection period of a decay of interest. GINA performs multiple functions related solely to the radioactive isotopes at the target location with other features relating to the isotopes being sent through the SuNTAN system. The GINA program uses a Graphical User Interface (GUI) programmed to work with up to four generations of decay, and the method used is generalized to work with any decay chain.

First, GINA calculates the number of radioactive isotopes at a target location based on some initial and constant rate of isotope implantation over some time. Let N denote the number of radioactive isotopes at a location and $T_{1/2}$ denote the half-life of a nucleus. Suppose we allow the superscript to denote the generation as a number, where (0) refers to the mother nucleus, (1) the daughter nucleus, (2) the granddaughter nucleus and so on such that (i) would represent the i^{th} generation nucleus. The number of mother nuclei only depends on the number of implanted nuclei and the number of nuclei that have decayed over some small amount of time Δt. If the total amount of elapsed time for a system is given by $n\Delta t$, where $n \in \mathbb{N}$ ($n = 1, 2, 3, \dots$), then one can represent the number of existing nuclei at any point by

$$N_n^{(0)} = N_1^{(0)} + N_{n-1}^{(0)} e^{-\frac{\Delta t}{T_{1/2}^{(0)}} \ln(2)}. \tag{3}$$

Representing the values in a series such as this was useful for programming purposes.

Next, for a later generation, the number of nuclei will depend on how many of that generation's nuclei decayed as well as how many of the previous generation's nuclei decayed into it. This gives

$$N_n^{(i)} = N_{n-1}^{(i-1)} \left(1 - e^{-\frac{\Delta t}{T_{1/2}^{(i-1)}} \ln(2)}\right) + N_{n-1}^{(i)} e^{-\frac{\Delta t}{T_{1/2}^{(i)}} \ln(2)}. \tag{4}$$

If it is assumed that the last stage has a near infinite half-life, the limiting case will produce a final step of this chain to be equivalent to

$$N_n^{last} = N_{n-1}^{last} + N_{n-1}^{d} \left(1 - e^{-\frac{\Delta t}{T_{1/2}^{last-1}} \ln(2)}\right). \tag{5}$$

These relations can be proven by induction and are demonstrated in Fig. 4 for the example chain ^{42}S $\rightarrow$ ^{42}Cl $\rightarrow$ ^{42}Ar.

During the experiment, the important number is not necessarily the number of nuclei but the number of decays. Therefore, GINA uses this information to determine the radioactive decay rates

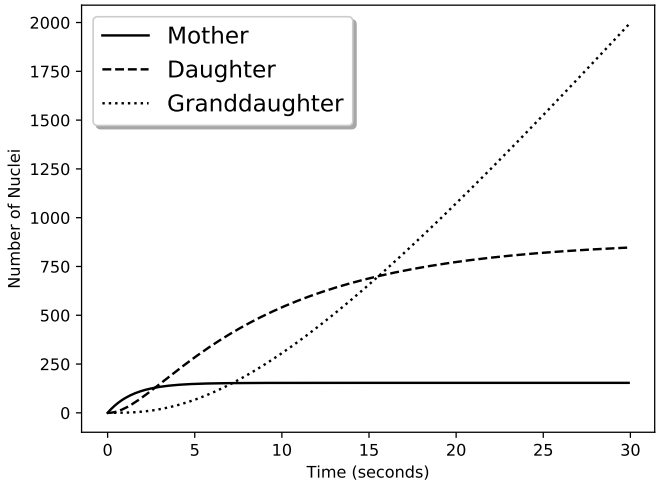

Figure 4. Using an input rate of 100 particles per second, this demonstrates the total nuclei count for an implanted isotope (as generated by the GINA program) of ^{42}S (solid line) which decays into ^{42}Cl (dashed line) and ^{42}Ar (dotted line).

of each isotope at the implantation point. The values N_n^0, and N_n^i all represent a total number of particles of a specific isotope. Eq. 1 defines the decay rate of an isotope. Using the total particle numbers calculated in Eq. 3 - 5, one can determine the decay rate to be

$$D_n^i = \frac{dN_n^i}{dt} = \frac{N_n^i \ln(2)}{T_{1/2}^i}. \tag{6}$$

These represent the total decays per second and are demonstrated in Fig. 5.

Finally, GINA does a calculation of the contamination on the implantation point relative to the primary isotope. The contamination is defined as the number of decays the non-primary isotopes are producing with respect to the number of decays the mother nuclei are producing. The contamination can be expressed as a percentage using

$$C_n = \frac{1}{D_n^{(0)}} \sum_{k=1}^{\infty} D_n^{(k)} \times 100\%. \tag{7}$$

Following this, another useful value to determine proper experimental parameters using the tape station is the deposited implant loss, L. This is the total percentage of implanted particles that have decayed and is given by

$$L_n = \frac{1}{nN_1^{(0)}} \sum_{k=i+1}^{\infty} N_n^{(k)}. \tag{8}$$

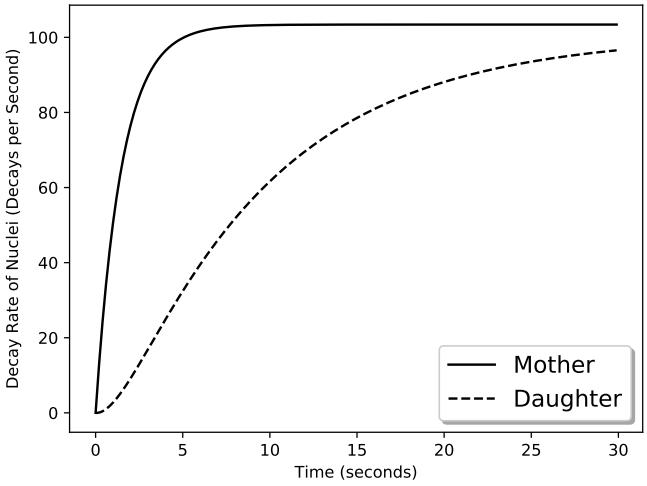

Figure 5. Using an input rate of 100 particles per second, this demonstrates the total nuclei decay rate (as generated by the GINA program) for an implanted isotope of ^{42}S (solid line) which decays into ^{42}Cl (dashed line) and approximating ^{42}Ar to be stable.

Both of these values are demonstrated in Fig. 6.

From the sequences listed above, the only needed inputs are the half-lives of each isotope. Because of this, GINA takes the half-lives of the primary isotope and each generation isotope up to four isotopes as initial input values. These are what is used to perform the calculations described above and no other values are needed. For the case of ^{42}S, one can see how the contamination percentage increases over time. The acceptable amount of contamination can be determined based on the detectors and methods being used for the specific setup as it was for the SuNTAN commissioning experiment.

4. CONCLUSION

Future experiments using SuNTAN have been planned and the GINA program is available and ready to use for the preparation of these experiments [12]. The program is not limited to use with SuNTAN and is made to be easily adapted for use with an arbitrary number of generations within a decay chain. The GINA program along with SuNTAN will help to further increase the understanding of the r-process and will lead to the study of isotopes that have not been studied previously.

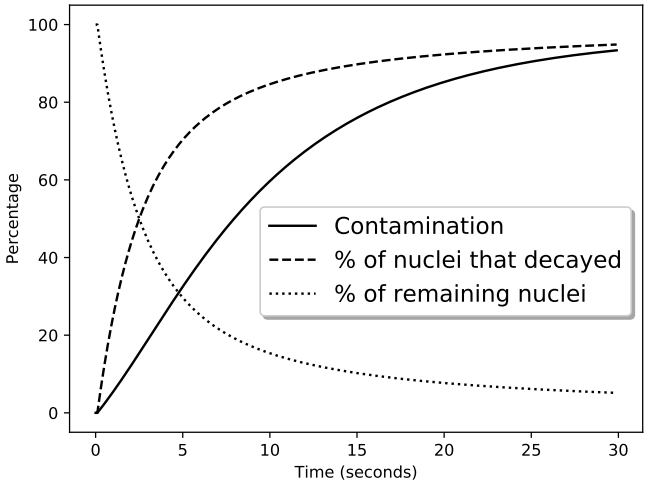

Figure 6. This demonstrates the total nuclei contamination (solid line) rate and implantation loss (dashed line), as generated by the GINA program, for an implanted isotope of ^{42}S which decays into ^{42}Cl and approximating ^{42}Ar to be stable.

5. ACKNOWLEDGMENTS

This work was supported by the National Science Foundation under Grants No. PHY 1102511 (NSCL) and No. PHY 1430152 (Joint Institute for Nuclear Astrophysics - Center for the Evolution of the Elements), and PHY 1350234 (CAREER). This material is based upon work supported by the Department of Energy/ National Nuclear Security Administration under Award Numbers DE-NA0003221, and DE-NA-0002132.

References

[1] E. M. Burbidge, G. R. Burbidge, W. A. Fowler, and F. Hoyle, Rev. Mod. Phys. 29, 547 (1957).

[2] F. Kappeler, Nuclear Instruments and Methods in Physics Research Section B: Beam Interactions with Materials and Atoms 259, 663 (2007), accelerator Mass Spectrometry.

[3] A. Spyrou, S. N. Liddick, F. Naqvi, B. P. Crider, A. C. Dombos, D. L. Bleuel, B. A. Brown, A. Couture, L. Crespo Campo, M. Guttormsen, A. C. Larsen, R. Lewis, P. Möller, S. Mosby, M. R. Mumpower, G. Perdikakis, C. J. Prokop, T. Renstrøm, S. Siem, S. J. Quinn, and S. Valenta, Phys. Rev. Lett. 117, 142701 (2016).

[4] T. Rauscher, N. Dauphas, I. Dillmann, C. Fröhlich, Z. Flöp, and G. Gyürky, Reports on Progress in Physics 76, 066201 (2013).

[5] M. Mumpower, R. Surman, G. McLaughlin, and A. Aprahamian, Progress in Particle and Nuclear Physics 86, 86 (2016).

[6] A. Simon, S. Quinn, A. Spyrou, A. Battaglia, I. Beskin, A. Best, B. Bucher, M. Couder, P. DeYoung, X. Fang, J. Grres, A. Kontos, Q. Li, S. Liddick, A. Long, S. Lyons, K. Padmanabhan, J. Peace, A. Roberts, D. Robertson, K. Smith, M. Smith, E. Stech, B. Stefanek, W. Tan, X. Tang, and M. Wiescher, Nuclear Instruments and Methods in Physics Research Section A: Accelerators, Spectrometers, Detectors and Associated Equipment 703, 16 (2013).

[7] S. N. Liddick, A. Spyrou, B. P. Crider, F. Naqvi, A. C. Larsen, M. Guttormsen, M. Mumpower, R. Surman, G. Perdikakis, D. L. Bleuel, A. Couture, L. Crespo Campo, A. C. Dombos, R. Lewis, S. Mosby, S. Nikas, C. J. Prokop, T. Renstrom, B. Rubio, S. Siem, and S. J. Quinn, Phys. Rev. Lett. 116, 242502 (2016).

[8] B. N. Laboratory, National Nuclear Data Center." https://www.nndc.bnl.gov/chart/, [Online; accessed 10-August-2018].

[9] P. Dam, E. Hagberg, and B. Jonson, Nuclear Instruments and Methods 161, 427 (1979).

[10] A. Mitchell, P. Bertone, B. DiGiovine, C. Lister, M. Carpenter, P. Chowdhury, J. Clark, N. DOlympia, A. Deo, F. Kondev, E. McCutchan, J. Rohrer, G. Savard, D. Seweryniak, and S. Zhu, Nuclear Instruments and Methods in Physics Research Section A: Accelerators, Spectrometers, Detectors and Associated Equipment 763, 232 (2014).

[11] C. Prokop, S. Liddick, B. Abromeit, A. Chemey, N. Larson, S. Suchyta, and J. Tompkins, Nuclear Instruments and Methods in Physics Research Section A: Accelerators, Spectrometers, Detectors and Associated Equipment 741, 163 (2014).

[12] A. Torode, GINA: Generations of Implanted Nuclear Activity," https://github.com/torodean/ Antonius-GINA (2018), [Online; accessed 10-August- 2018].

Effective Density of Crumpled Paper Balls

Tarush Bansal[1*], Aayush Chowdhry[1], Gyaneshwaran Gomathinayagam[2#]**

[1]12th Grade, The Doon School, Mall Road, Dehradun- 248001, Uttrakhand
[2]M.Sc. Department of Physics, The Doon School, Mall Road, Dehradun- 248001, Uttrakhand

Abstract: The physics of the crumpling of paper balls is quite complex and is not yet fully understood. Researchers have studied the 3D structure of crumpled paper balls using advanced experimental techniques like X-ray micro-tomography and discovered that crumpling is similar to other classic non-equilibrium problems like turbulence and very difficult to model mathematically. We have investigated how the diameter of paper balls obtained by crumpling square sheets of paper of different areas by hand, depends on the side-length of the paper. Our first model which assumed the density of the paper ball to be equal to the density of the paper used failed by predicting the wrong thickness of paper used. However, our second model which only equated the mass of the paper used to the mass of the paper ball obtained, and allowed for the effective density of the crumpled paper ball to be different from the density of paper used was successful in predicting the correct thickness of the paper. From this observation, we concluded that the paper balls obtained from crushing by hand have a lower (around 3 times) constant effective density than the density of paper. If useful applications could be found for crushed paper balls, which have many interesting properties like low density with high compressive strength and energy-absorbing properties, they could provide useful solutions for paper-waste management.

Keywords: *paper ball, crumpling, effective density*

1. INTRODUCTION

Academic institutions and corporate offices do a lot of paper work and generate a lot of paper waste. Recycling the paper by turning it back to pulp is one way of managing this waste. However, crumpled paper balls could also provide some alternative solutions for waste management since they have many interesting properties like high strength to weight characteristics, high compressive strength and high energy-absorbing properties [1] opening the possibilities for many innovative applications.

Earlier studies on crumpled paper balls have tried to model the 3D structure of crumpling using very advanced experimental techniques like X-ray micro-tomography [2] and laser-aided topography [3] or studied the shape, response and stability of conical dislocations, the simplest type of topological crumpling deformation [4]. Another study has established power-law dependence between the compaction force required to crumple a sheet into a ball and the diameter of the crumpled ball. In this study we investigate how the diameter of crumpled paper balls depends on the side-length of square sheets of paper used, by keeping the compaction force constant and equal to the maximum force that can be exerted by hand while crumpling the sheets of paper into a ball.

*jtarush.470.2019@doonschool.com, **aayush.467.2019@doonschool.com, #gya@doonschool.com

2. HYPOTHESIS

In the first hypothesis, we equated the volume of the sheet of paper to the volume of the paper ball by assuming the density of the crumpled paper balls to be equal to the density of the paper used.

$$l^2 t = \frac{4}{3}\pi\frac{d^3}{8} \qquad (1)$$

where l = length of side of square sheet of paper, t = thickness of sheet of paper, d = diameter of crumpled paper ball.

From equation (1), we obtain

$$d^3 = \left(\frac{6t}{\pi}\right) l^2 \qquad (2)$$

Thus, on plotting d^3 vs l^2, we should obtain a linear graph passing through the origin, and we should be able to calculate the thickness of the sheet of paper used from the slope of the graph. If it agrees with the actual thickness of the sheet of paper measured directly (0.00992 ± 0.00002 cm), then we can conclude that the hypothesis is correct.

In the second hypothesis, we equate only the mass of the sheet of paper to the mass of the paper ball.

$$\rho_p l^2 t = \rho_b \frac{4}{3}\pi\frac{d^3}{8} \qquad (3)$$

where ρ_p = measured density of paper sheet = 0.78 ± 0.02 g.cm^{-3}, ρ_b = effective density of crumpled paper ball.

From equation (3), we obtain

$$d^3 = \left(\frac{\rho_p}{\rho_b}\right)\left(\frac{6t}{\pi}\right) l^2 \qquad (4)$$

The second hypothesis predicts a larger value for the slope of the linear fit if the effective density of the paper balls is lesser than the actual density of the sheets of paper used to make the crumpled paper balls. The thickness of the sheets of paper calculated using this value of slope should give a different value and thus can be used to identify the correct hypothesis by comparing it with the actual measured value of thickness of paper.

3. METHODS

Identical A3 sheets of paper were taken and cut into 40 square pieces (5 sets of eight different side-lengths). The square pieces of paper were crumpled into spherical paper balls by applying the maximum force possible by hand. The compacting force applied to make the crumpled paper balls was made constant in this way. The diameter of each paper ball was then measured using vernier caliper or screw gauge. (see Figure 1)

Figure 1. Measuring the diameter of crumpled paper balls

The density ρ_p of the sheets of paper used to make the crumpled paper balls was calculated to be 0.78 ± 0.02 gcm^{-3} by first measuring the mass of the biggest square piece of paper and dividing the mass by its volume. The thickness of a single sheet of paper,'t' was calculated to be 0.00992 ± 0.00002 cm by measuring the thickness of a pile of 48 sheets of paper using a screw gauge. The effective density of the crumpled paper ball for each diameter of crumpled paper ball was calculated using the mass per unit area and area of the sheet of paper used to make the paper ball, and the mean diameter of the crumpled paper ball.

4. RESULTS AND DISCUSSION

Figure 2 shows that the effective density of the crumpled paper balls does not depend on their diameter. The data point for the smallest paper ball is an outlier and the error could be due to the fact that its diameter was measured using a screw gauge whereas the diameters of all the other paper balls were measured using vernier calliper. The paper ball could have been crushed more during the process of measuring the mean diameter using screw gauge, causing the error.

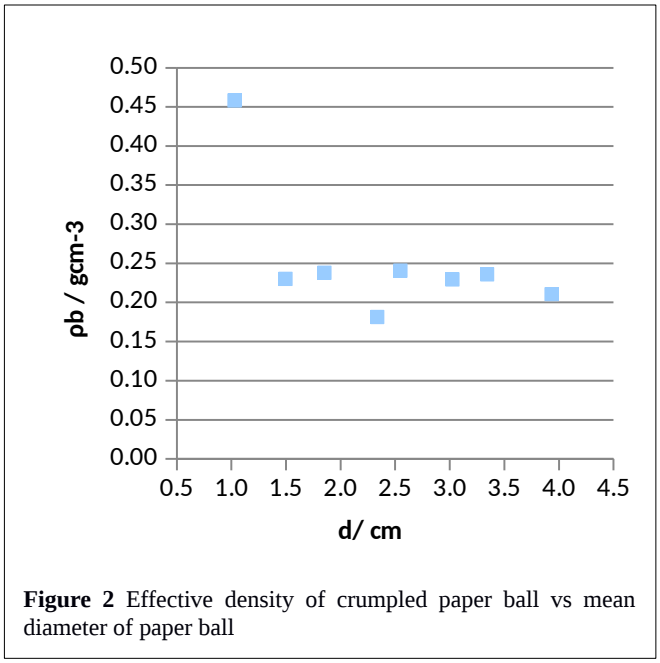

Figure 2 Effective density of crumpled paper ball vs mean diameter of paper ball

The mean effective density of the crumpled paper balls ρ_b was found to be 0.25 ± 0.06 gcm^{-3} which is much less than the density ρ_p of the sheets of paper used to make the crumpled paper balls.

Thus, hypothesis 1 has been proven to be invalid, since it assumed the density of the crumpled paper balls to be equal to the density of paper.

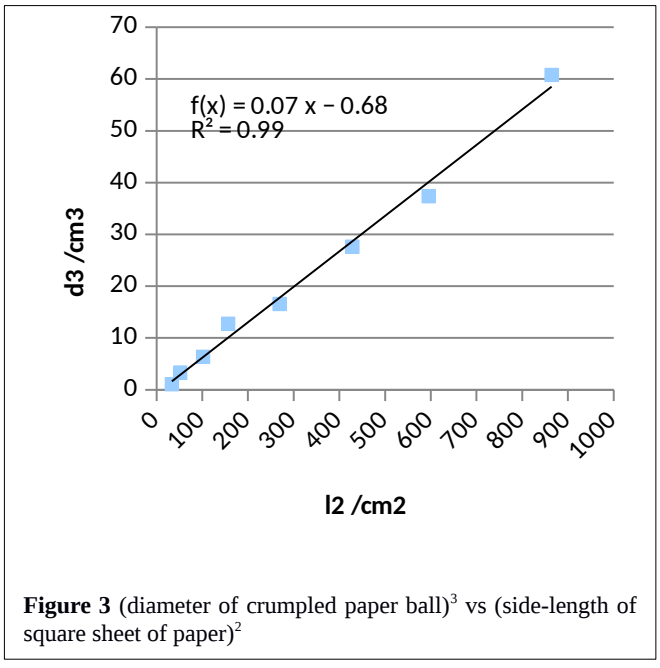

Figure 3 (diameter of crumpled paper ball)^3 vs (side-length of square sheet of paper)^2

Figure 3 shows that the linear best-fit straight line passing through the origin as predicted by hypothesis 2. Furthermore, the thickness of the sheet of paper calculated from the slope of the linear best-fit straight line by using the correcting factor $\frac{\rho_p}{\rho_b} = 3.09$,which takes into account the reduced effective density of the crumpled paper balls was found to be 0.012 ± 0.006 cm which is in very good agreement with 0.00992 ± 0.00002cm (the measured thickness of 1 sheet of paper). The uncertainty in the diameter of the crumpled paper balls was found to increase with the size of the paper balls because bigger paper balls would not acquire a perfectly spherical shape, and would compress more during the measurement process causing variation in the measured values for each trial.

For further research, a similar study could be conducted for balls made of strings or ribbons of different materials like wool, cotton, silk, etc by first soaking them in a liquid adhesive and then removing the excess adhesive by allowing it to drip away during compression. Their material properties like effective density, compressive strength and energy-absorbing properties could be studied.

5. CONCLUSION

The effective density of crumpled paper balls (0.25 ± 0.06 gcm^{-3}) was found to be around 3 times smaller than the density of paper (0.78 ± 0.02 gcm^{-3}) used to make them by compacting at maximum pressure that could be exerted by hand, for square sheets of paper of side-lengths ranging from 6 cm to 30 cm. The effective density of crumpled paper balls does not depend on the area of paper used or the diameter of the crumpled paper balls formed. It depends only on the maximum compacting force applied to crumple and make the paper balls, which was a constant in this investigation and equal to the maximum force that could be exerted by hand. The variation in maximum force exerted by a 17 year old male teenager or a male adult while making a crumpled paper ball by hand did not cause any significant change in the mean diameter of the crumpled paper ball. Further investigation may be carried out by crumpling the paper balls using a machine which can exert a known maximum force. The dependence of the effective density of the crumpled paper balls on the maximum force applied during crumpling could then be confirmed. The maximum force applied to make the crumpled paper balls can be varied over a wide range using a machine. Pieces of paper having smaller area may be used to investigate whether the anomalous data point corresponding to paper of area 33.4 cm^2 was really an anomaly or a trend.

References

[1] D.A.H. Hanaor, E.A. Flores Johnson, S. Wang,S. Quach, K.N. Dela-Torre,Y. Gan, L. Shen. Mechanical properties in crumple-formed paper derived materials subjected to compression. Heliyon 3 (2017) e00329.doi: 10.1016/j.heliyon.2017.e00329

[2] "Three-dimensional structure of a sheet crumpled into a ball." By Anne Dominique Cambou and Narayanan Menon. Proceedings of the National Academy of Science, Vol. 108 No. 33, August 23, 2011.

[3] Blair, Daniel L., and Arshad Kudrolli. “Geometry of Crumpled Paper.” Physical Review Letters, vol. 94, no. 16, 2005, doi:10.1103/physrevlett.94.166107.

[4] Cerda, Enrique, et al. “Conical dislocations in crumpling.” Nature, vol. 401, no. 6748, 1999, pp. 46–49., doi:10.1038/43395.

STUDENT JOURNAL OF PHYSICS

Volume 7 **Number 1** **Jan - Mar 2018**

CONTENTS

ARTICLES

Networks of topological string defects with different Non-Abelian fundamental groups 1
Ramyak Bilas

Machine Learning Applied to Multi-Electron Events in Scintillator 18
Harrison LaBollita, Morten Hjorth – Jensen, Sean Liddick

Real Space Renormalization Group for One-Dimensional Ising Chains 26
Shraddha Singh, Vijay Singh

Software Development to Determine the Optimal Parameters of a Tape Transport System 35
A. Torode, M. K. Smith, A. Spyrou, C. Harris, S. Lyons, A. C. Dombos, S. N. Liddick

Effective Density of Crumpled Paper Balls 45
Tarush Bansal, Aayush Chowdhry, Gyaneshwaran Gomathinayagam